Multiwavelength constraints on the origin of a nearby repeating fast radio burst source in a globular cluster

A list of authors and their affiliations appears at the end of the paper

The precise origins of fast radio bursts (FRBs) remain unknown. Multiwavelength observations of nearby FRB sources can provide important insights into the enigmatic FRB phenomenon. Here we present results from a sensitive, broadband X-ray and radio observational campaign of FRB 20200120E, the closest known extragalactic repeating FRB source (located 3.63 Mpc away in an ~10-Gyr-old globular cluster). We place deep limits on the persistent and prompt X-ray emission from FRB 20200120E, which we use to constrain possible origins for the source. We compare our results with various classes of X-ray sources, transients and FRB models. We find that FRB 20200120E is unlikely to be associated with ultraluminous X-ray bursts, magnetar-like giant flares or an SGR 1935+2154-like intermediate flare. Although other types of bright magnetar-like intermediate flares and short X-ray bursts would have been detectable from FRB 20200120E during our observations, we cannot entirely rule them out as a class. We show that FRB 20200120E is unlikely to be powered by an ultraluminous X-ray source or a young extragalactic pulsar embedded in a Crab-like nebula. We also provide new constraints on the compatibility of FRB 20200120E with accretion-based FRB models involving X-ray binaries. These results highlight the power of multiwavelength observations of nearby FRBs for discriminating between FRB models.

FRBs are energetic, short-duration bursts of coherent radio emission[1] that typically emanate from objects located well outside the Milky Way[2,3]. A wide variety of models have been proposed to explain the origins of FRBs[4]. However, models involving magnetars are presently favoured[5,6].

FRBs and Galactic radio magnetars have been observed to produce radio emission with strikingly similar characteristics[7–10]. The strongest link between FRBs and magnetars was established when an FRB-like radio burst was detected from the Galactic magnetar SGR 1935+2154 on 28 April 2020[8,9], demonstrating that similar events could be detectable from extragalactic distances. A short X-ray burst was also detected near the time of this FRB-like radio burst from SGR 1935+2154 (refs. 11–14). The spectrum of the X-ray burst was harder than other short X-ray bursts detected from SGR 1935+2154 (refs. 11,13), but it was not unusually energetic relative to other short X-ray bursts from

Galactic magnetars. These observations suggest that some fraction of the cosmological FRB population may be powered by extragalactic, X-ray-emitting magnetars.

FRB 20200120E was discovered using the Canadian Hydrogen Intensity Mapping Experiment (CHIME) radio telescope and the CHIME/FRB system[15,16]. Using radio telescopes from the European Very Long Baseline Interferometry (VLBI) Network (EVN), FRB 20200120E was subsequently localized to an ~10-Gyr-old globular cluster within the M81 galactic system using VLBI[17].

FRB 20200120E is the nearest known extragalactic repeating FRB source. Previous simultaneous X-ray and radio observations of more distant FRB sources (for example, see refs. 18–20) have been unable to rule out most viable FRB source types because of the sensitivity limitations of current X-ray instruments. In addition, the radio bursts
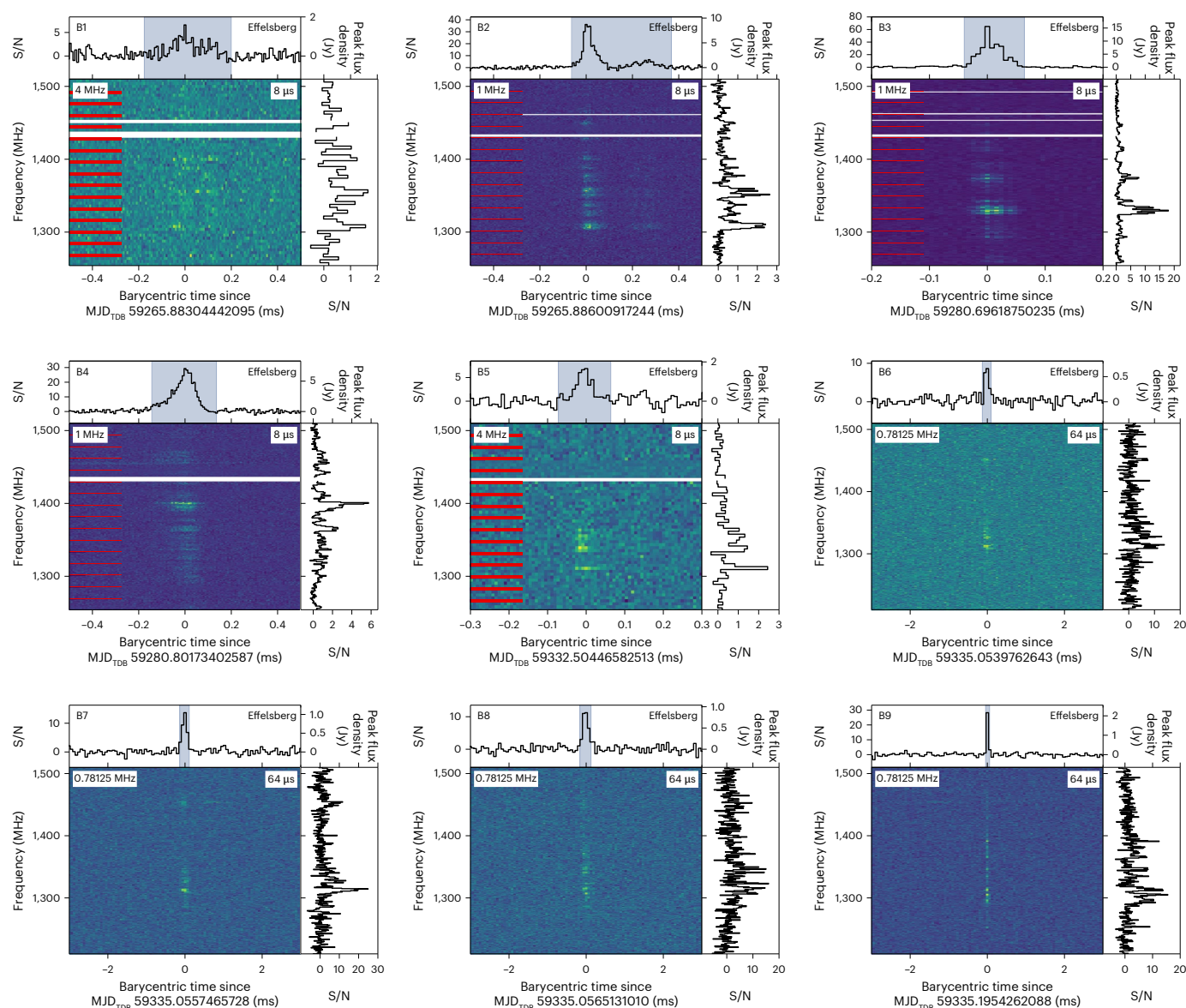
Fig. 1 | Radio bursts detected from FRB 20200120E using the Effelsberg radio telescope. Top panels: total intensity (Stokes I) frequency-summed burst profiles. The shaded blue region in the top panels corresponds to the $\pm 2\sigma$ burst width, which was used to calculate the S/N and peak flux density. Middle panels: dynamic spectra of the radio bursts. For bursts B1–B5, the red lines mark the edges of the individual 16-MHz subbands, and the white lines indicate frequency channels that were masked to mitigate RFI. Right panels: time-averaged frequency spectra of the bursts. The time resolution and frequency resolution of the data are labelled in the top right and top left corners of the middle panels, respectively.

detected from FRB 20200120E sometimes display pulse components with widths of ~10–100 ns (refs. 21,22), which is the shortest-duration radio emission observed from an FRB source so far. These previous X-ray studies[18–20] have not searched for prompt X-ray emission from FRBs on such ultrashort timescales.

In this Article, we present results from a simultaneous X-ray and radio observing campaign of FRB 20200120E, which yielded the deepest persistent and prompt X-ray luminosity limits from an FRB source so far in the soft X-ray band. We derive constraints on the possible origins of FRB 20200120E and compare our results with various types of X-ray sources, transients and predictions for multiwavelength emission from different FRB models.

Observations

High-time-resolution radio observations of FRB 20200120E were carried out using the Effelsberg 100-m and CHIME radio telescopes. We recorded radio data at a central frequency of 1.4 GHz with Effelsberg and in the 400–800 MHz frequency range using the CHIME/Pulsar system (Methods). We also performed X-ray observations of FRB 20200120E using the Neutron Star Interior Composition Explorer (NICER), XMM-Newton, Chandra and NuSTAR (Methods). These observations were coordinated to maximize our simultaneous X-ray and radio coverage of FRB 20200120E. A timeline of these observations is shown in Extended Data Fig. 1, and the observations are listed in Extended Data Tables 1 and 2.

Results

We detected nine radio bursts from FRB 20200120E during our Effelsberg observations. No radio bursts were detected during our CHIME/Pulsar observations. Throughout this Article, we label the radio bursts from FRB 20200120E as Bn, and they are ordered chronologically by their time of arrival (ToA). Bursts B1–B5 were detected during Pinpointing Repeating CHIME Sources with the EVN (PRECISE) VLBI observations of FRB 20200120E[17,22], and bursts B6–B9 were

Table 1 | 3σ X-ray fluence and X-ray energy upper limits from FRB 20200120E at the times of bursts B4 and B9, derived from NICER and XMM-Newton observations

Timescale (Δt)	N^a_{obs} (Counts)	Absorbed 0.5–10 keV Fluence limit (Model 1[b]): $\Gamma = 1.5$, $E_{cut} = 85$ keV ($\mathscr{F}_X$, 10^{-10} erg cm^{-2})	Absorbed 0.5–10 keV Fluence limit (Model 2[c]): $kT = 10$ keV ($\mathscr{F}_X$, 10^{-10} erg cm^{-2})	Absorbed 0.5–10 keV Fluence limit (Model 3[d]): $\Gamma = -0.5$, $E_{cut} = 500$ keV ($\mathscr{F}_X$, 10^{-10} erg cm^{-2})	Unabsorbed 0.5–10 keV Energy limit[e] (E_X, 10^{41} erg)
NICER upper limits at the time of burst B4					
10 s	7	<0.4	<3	<3	<0.5–5
1 s	1	<0.3	<2	<2	<0.3–3
100 ns to 100 ms[f]	0	<0.2	<1	<1	<0.3–2
XMM-Newton upper limits at the time of burst B9					
100 s	1	<0.4	<1	<1	<0.6–2
100 ms to 10 s[g]	0	<0.3	<1	<1	<0.5–2

X-ray fluence and X-ray energy upper limits are derived from Poisson 3σ (99.73%) confidence intervals, calculated using the Bayesian method described in ref. 89. The background measurements in Extended Data Table 4 were used to obtain confidence intervals for NICER. [a]The number of photons detected with NICER or XMM-Newton in the 0.5–10 keV energy band within ±Δt/2 of the barycentric, infinite frequency peak time of burst B4 (t^{B4}_{peak}) or burst B9 (t^{B9}_{peak}). The number of photons reported for XMM-Newton are within the PSF of the EPIC/pn camera, which was centred on FRB 20200120E's position from VLBI[17]. [b]Model 1 corresponds to an exponentially cut-off power-law spectrum, similar to the X-ray counterpart of the FRB-like radio burst from SGR 1935+2154 (refs. 11–14). [c]Model 2 corresponds to a typical blackbody spectrum observed from magnetar hard X-ray bursts[119,120]. [d]Model 3 corresponds to an exponentially cut-off power-law spectrum, similar to the spectrum measured from the SGR 1806–20 giant flare[31,121]. [e]The unabsorbed energy limits were calculated assuming a distance of 3.63±0.34 Mpc (ref. 122) to FRB 20200120E. The range indicates the minimum and maximum values obtained using the unabsorbed fluence limits from models 1, 2 and 3. [f]The absorbed fluence and unabsorbed energy limits were calculated on timescales of 100 ns, 1 μs, 10 μs, 100 μs, 1 ms, 10 ms and 100 ms. Identical values were obtained for these timescales. [g]The absorbed fluence and unabsorbed energy limits were calculated on timescales of 100 ms, 1 s and 10 s. Identical values were obtained for these timescales.

detected during target of opportunity (ToO) observations of FRB 20200120E with Effelsberg (Methods). The dynamic spectra, burst profiles and frequency spectra of these radio bursts are shown in Fig. 1. We provide measurements of the radio burst properties in Extended Data Table 3.

Burst B4 occurred during a simultaneous NICER exposure (Extended Data Fig. 2a), and it was the most energetic radio burst detected. Together with measurements from NICER (Table 1, Extended Data Figs. 2 and 3 and Extended Data Table 4), it provides the best constraints on prompt X-ray emission from FRB 20200120E. The radio burst profiles of B4 are shown in Extended Data Fig. 2b–d at time resolutions of 8 μs, 1 μs and 31.25 ns, along with the barycentric time separations of the nearest photons from the peak of the radio burst. The nearest photon detected by NICER in the 0.5–10 keV band occurred ~300 ms before the barycentric, infinite frequency peak time of burst B4.

Bursts B6–B9 were detected during simultaneous ToO X-ray observations with XMM-Newton. The 0.5–10 keV XMM-Newton EPIC/pn light curves from these observations are shown in Extended Data Fig. 4a, along with the ToAs of bursts B6–B9 (Extended Data Table 3). The burst profiles of B6–B9, times of the nearest photons and their barycentric time separations from the peaks of the radio bursts are shown in Extended Data Fig. 4b–e. Bursts B6–B8 occurred during times of high background flaring, so we provide prompt X-ray limits using XMM-Newton EPIC/pn measurements at the time of burst B9 only. The nearest photon occurred 58.4 s before the barycentric, infinite frequency peak time of burst B9.

We did not detect any statistically significant increase in X-ray emission near the times of bursts B1–B9 that could be attributed to FRB 20200120E. We also carried out a search for periodic X-ray pulsations but did not detect evidence of pulsed X-ray emission (Methods). In Table 1, we list 3σ upper limits on the 0.5–10 keV X-ray fluence and X-ray energy at the times of bursts B4 and B9. For B4, we calculated X-ray fluence limits using measurements from NICER on 100 ns to 10 s timescales. X-ray fluence limits were also calculated for burst B9 on 100 ms to 100 s timescales using measurements from XMM-Newton's EPIC/pn camera. The X-ray fluence limits were derived using standard 3σ confidence intervals (Methods) and several fiducial spectral models that have been used to characterize prompt high-energy emission from magnetars (Table 1).

In Fig. 2, we show our limits on the energy of 0.5–10 keV X-ray bursts at the times of bursts B4 and B9. For comparison, we also show previous limits from simultaneous X-ray and radio observations at the times of radio bursts detected from FRB 20121102A and FRB 20180916B[19,23], along with the fiducial spectral models used in Table 1. Figure 2 illustrates that our prompt X-ray burst energy limits are ~10^4 times deeper than the X-ray limits obtained from the next nearest known repeating FRB source (FRB 20180916B) for which such limits have been placed.

In Extended Data Table 5, we list X-ray fluences for the X-ray burst associated with the FRB-like radio burst detected from SGR 1935+2154 on 28 April 2020, based on measurements from AGILE[14], Insight-HXMT[12], INTEGRAL[11] and Konus-Wind[13]. We also derive X-ray fluences in the 0.5–10 keV and 3–79 keV energy bands for an identical burst emitted from the location of FRB 20200120E.

In Fig. 3, we compare the X-ray and radio fluences of bursts from SGR 1935+2154 with other magnetars, previous limits from simultaneous X-ray and radio observations of repeating and non-repeating extragalactic FRBs, and our measurements from FRB 20200120E. The radio and X-ray fluences (or fluence limits) are shown in Fig. 3a, and the corresponding isotropic-equivalent radio and X-ray energies (or energy limits) are plotted in Fig. 3b. Figure 3 shows that our prompt X-ray fluence and X-ray energy limits from FRB 20200120E are deeper than all previous measurements from FRB sources.

We provide 3σ persistent X-ray flux limits during each of our observations of FRB 20200120E with Chandra, NICER, NuSTAR and XMM-Newton in Extended Data Table 2. The corresponding persistent X-ray luminosity limits are shown in Fig. 4a. We show the X-ray luminosity distributions of ultraluminous X-ray (ULX) sources, low-mass X-ray binaries (LMXBs), high-mass X-ray binaries (HMXBs) and magnetars in Fig. 4b (Methods), along with our persistent X-ray luminosity limits derived from our observations of FRB 20200120E. Potential source types for FRB 20200120E with higher persistent X-ray luminosities than our limits are ruled out at the times of our X-ray observations.

In Fig. 5, we show the absorbed 0.5–10 keV X-ray fluences of different types of prompt emission from potential X-ray counterparts to FRBs, after translating to the distance of FRB 20200120E and accounting for the Galactic line-of-sight hydrogen column density ($N_H = 6.73 \times 10^{20}$ cm^{-2})[24].
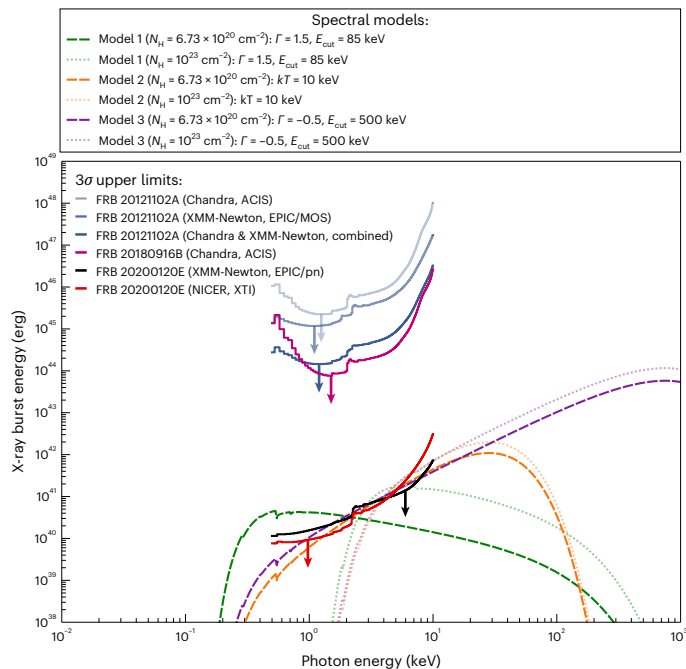
Fig. 2 | Limits on the energy of X-ray bursts between 0.5 and 10 keV at the times of radio bursts from FRB 20200120E, FRB 20121102A and FRB 20180916B. The red curve shows the 3σ limits derived from NICER observations of FRB 20200120E at the time of burst B4, after incorporating the spectral response of the NICER XTI. The black curve shows the 3σ limits derived from XMM-Newton observations of FRB 20200120E at the time of burst B9, after including the spectral response of the XMM-Newton EPIC/pn camera. The light-blue curves correspond to previous 3σ limits derived from Chandra and XMM-Newton observations at the times of multiple radio bursts from FRB 20121102A[23]. Stacked 3σ limits for FRB 20121102A are shown in dark blue. The magenta curve shows previous 3σ limits derived from a Chandra observation at the time of a radio burst from FRB 20180916B[19]. Several fiducial spectral models are shown for comparison. The green curves correspond to exponentially cut-off power-law spectra with $\Gamma = 1.5$ and $E_{cut} = 85$ keV, similar to the X-ray counterpart associated with the FRB-like radio burst detected from SGR 1935+2154 on 28 April 2020[11–14]. The orange curves represent blackbody spectra with $kT = 10$ keV, which have been observed from some magnetar hard X-ray bursts[119,120]. The purple curves show exponentially cut-off power-law spectra with $\Gamma = -0.5$ and $E_{cut} = 500$ keV, similar to the spectrum observed during SGR 1806–20's giant flare[31,121]. The dashed spectra were calculated using a hydrogen column density of $N_H = 6.73 \times 10^{20}$ cm^{-2} towards FRB 20200120E[24], and the dotted spectra were calculated using a hydrogen column density of $N_H = 10^{23}$ cm^{-2} to illustrate the effects of high absorption local to the source. Larger hydrogen column densities yield harder X-ray spectra, with increased absorption at lower X-ray energies. Although high absorption towards FRB 20200120E is not expected, this scenario is shown for comparison. Each fiducial X-ray spectrum was normalized such that the integrated X-ray burst energy in the 0.5–10 keV energy range is equal to the NICER 0.5–10 keV band-averaged energy limit from FRB 20200120E.

We refer to each translated X-ray fluence value as a 'pseudo-fluence', since it corresponds to the X-ray fluence for an identical event emitted from the location of FRB 20200120E. To derive these pseudo-fluences, we translated each reported X-ray fluence to the 0.5–10 keV energy band using the XSPEC spectral fitting software package[25] and the best-fit spectral model reported for each burst or flare (Methods). We show the pseudo-fluence distributions of magnetar giant flares, intermediate flares and short bursts in Fig. 5, along with the distribution of type I X-ray bursts from LMXBs. We also label the X-ray pseudo-fluences of gamma-ray bursts (GRBs) from extragalactic magnetar giant flares, ultraluminous X-ray bursts (ULXBs) from unknown objects in extragalactic globular clusters, bright type II X-ray bursts from LMXBs and predictions from the relativistic shock

model described in refs. 26,27 (Supplementary Information). Our best prompt 3σ X-ray fluence limit for FRB 20200120E, derived from NICER measurements on 100 ns to 100 ms timescales at the time of burst B4, is also shown for comparison.

Discussion

Here, we compare our results to various types of X-ray sources and transients, as well as predictions for multiwavelength emission from popular FRB models. In the Supplementary Information, we consider other possible scenarios, compare our results with multiwavelength observations of other repeating FRBs, and discuss the prospects of future searches for X-ray emission from FRBs using current and future X-ray telescopes (Extended Data Fig. 5).
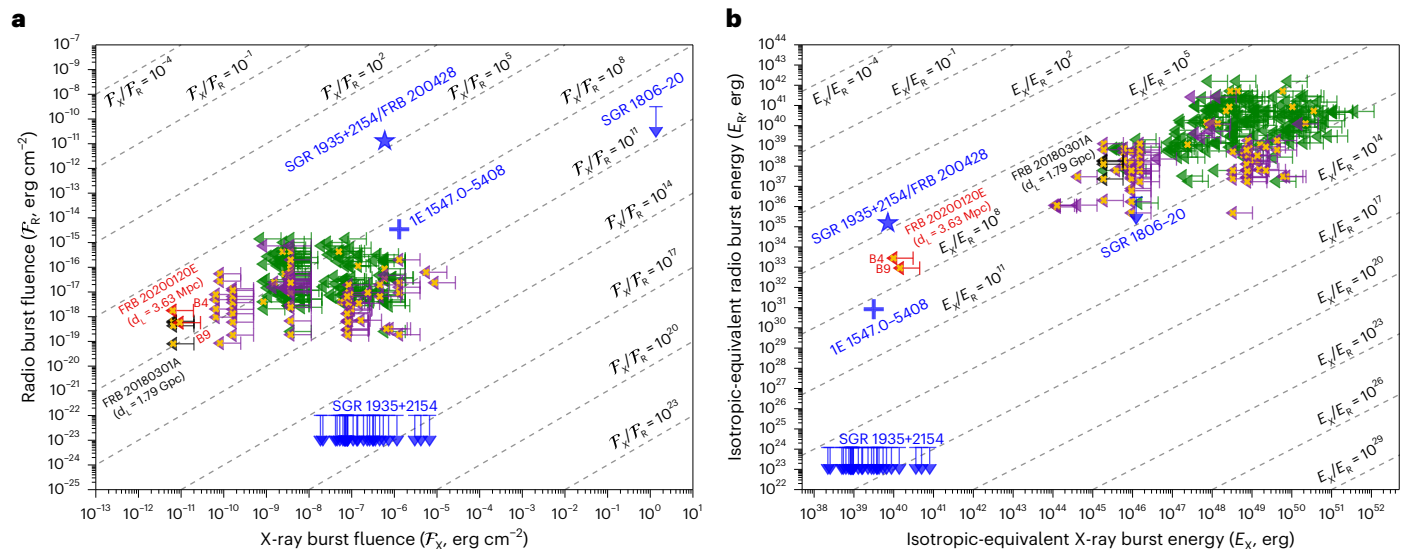
Magnetars

High-energy magnetar bursts are typically classified into three types, based on their phenomenology and energetics[28,29]: (1) giant flares (for example, see refs. 30,31), (2) intermediate flares (for example, see refs. 32,33) and (3) short bursts (for example, see refs. 34,35). Giant flares from magnetars have been detected with peak X-ray luminosities of $L_X \approx 10^{44}$–10^{48} erg s^{-1} and have durations of approximately a few hundred seconds, whereas intermediate flares have typical peak luminosities of $L_X \approx 10^{41}$–10^{43} erg s^{-1} and durations of a few seconds. Short magnetar bursts, on the other hand, have been detected with lower peak X-ray luminosities ($L_X \approx 10^{36}$–10^{41} erg s^{-1}) and durations ranging between a few milliseconds and a few seconds. We discuss the FRB–magnetar connection and the detectability of each of these transient radiative phenomena during our observations of FRB 20200120E.

An intermediate flare[36], short X-ray bursts[11–14] and FRB-like radio bursts[8,9] have been detected from SGR 1935+2154, suggesting that similar emission may be detectable from nearby FRB sources. We rule out the possibility that an intermediate flare, similar to the event detected on 12 April 2015 from SGR 1935+2154 (ref. 36), was produced from FRB 20200120E at the times of bursts B4 and B9. The 0.5–10 keV X-ray pseudo-fluence of the 12 April 2015 intermediate flare from SGR 1935+2154 is above our prompt 3σ X-ray fluence limits (Fig. 5 and Table 1), indicating that such a flare would have been detectable if it were emitted from FRB 20200120E. The predicted 0.5–10 keV X-ray fluence for a short X-ray burst similar to the one accompanying the FRB-like radio burst from SGR 1935+2154 on 28 April 2020 (Fig. 5 and Extended Data Table 5) is approximately an order of magnitude below our deepest 3σ X-ray fluence limit. However, X-ray bursts with larger ($\gtrsim 10\times$) fluences than this X-ray burst from SGR 1935+2154 have been observed[11] and would have been detectable from FRB 20200120E during our X-ray observations.

Archival X-ray observations of M81 with INTEGRAL, spanning nearly 18 years and covering the position of FRB 20200120E, have also been used to place shallow limits on powerful magnetar giant flares in the hard X-ray band[37], but not at times of simultaneous radio bursts. The absorbed X-ray pseudo-fluences of the magnetar giant flares from SGR 1806–20, SGR 1900+14 and SGR 0526–66 are well above our prompt X-ray fluence limits derived at the times of bursts B4 and B9 (Fig. 5 and Table 1). Thus, we rule out the possibility that a giant flare, similar to those observed from known magnetars, was produced from FRB 20200120E simultaneously with these radio bursts.

In Fig. 5, we show that most (~75%) of the magnetar intermediate flares detected so far have absorbed X-ray pseudo-fluences that are above our prompt 3σ X-ray fluence limits, derived at the times of bursts B4 and B9. Thus, similar intermediate flares would have been detectable during our observations of FRB 20200120E. A small fraction (~1%) of the most energetic magnetar short bursts also have absorbed X-ray pseudo-fluences that are above our prompt 3σ X-ray fluence limits, indicating that similar events also would have been detectable from FRB 20200120E. These include several bright short X-ray bursts from the radio magnetar 1E 1547.0–5408 (ref. 38), which has been observed

Fig. 3 | X-ray and radio burst fluence and energy limits from observations of FRB 20200120E, along with previous measurements from simultaneous X-ray and radio observations of FRB sources and Galactic magnetars. a, X-ray and radio fluence measurements of repeating FRB sources (purple), non-repeating FRB sources (green) and Galactic magnetars (blue). The red data points correspond to our X-ray and radio fluence measurements from NICER, XMM-Newton and Effelsberg observations of FRB 20200120E at the times of bursts B4 and B9. The black data points highlight X-ray and radio fluence measurements from observations of FRB 20180301A (luminosity distance of $d_L = 1.79$ Gpc) with NICER and the Five-hundred-meter Aperture Spherical radio Telescope (FAST)[20]. The blue star indicates the X-ray and radio fluences of the X-ray and radio bursts detected from SGR 1935+2154 during an episode of FRB-like activity on 28 April 2020[8,9,12]. The blue upper limits from SGR 1935+2154 show constraints on prompt radio emission from FAST observations during a

series of X-ray bursts detected with the Fermi Gamma-ray Burst Monitor on 28 April 2020, close in time to the FRB-like radio burst[123]. The blue cross corresponds to X-ray and radio measurements of an FRB-like burst from the radio magnetar 1E 1547.0−5408 (ref. [10]). The blue upper limit for SGR 1806−20 is derived from simultaneous radio and gamma-ray measurements at the time of the 27 December 2004 giant magnetar flare[124]. The dashed grey lines indicate constant X-ray-to-radio fluence ratios ($\mathcal{F}_X/\mathcal{F}_R$). **b**, X-ray and radio energy measurements of repeating FRB sources, non-repeating FRB sources and Galactic magnetars. The data points in **b** are derived from the same measurements shown in **a**. Radio and X-ray energies were calculated using the distance and redshift of each object. DM-inferred distances were used for unlocalized FRB sources. The dashed grey lines indicate constant X-ray-to-radio energy ratios (E_X/E_R). In **a** and **b**, the yellow crosses highlight measurements from localized FRB sources with measured redshifts.

to produce FRB-like radio bursts[10]. While we cannot entirely rule out the possibility that an intermediate flare or short magnetar burst was emitted from FRB 20200120E, since events below our X-ray fluence detection threshold would not have been detected during our observations because of limited X-ray telescope sensitivity, we are able to rule out prompt X-ray emission similar to some of the most energetic intermediate flares and short bursts detected thus far from the known magnetar population.

Magnetars have been detected with persistent X-ray luminosities ranging between approximately 10^{29} and 10^{36} erg s^{-1} in the soft X-ray band[39]. During bright outbursts, their persistent X-ray luminosities have been seen to reach up to ~10^{36} erg s^{-1} (ref. [40]). This maximum observed persistent X-ray luminosity is theoretically motivated by the dominance of neutrino cooling in the neutron star (NS) crust at high temperatures[41,42], so the persistent X-ray emission from magnetars is not expected to exceed this level. This maximum persistent X-ray luminosity is approximately five times fainter than the 3σ X-ray luminosity limit obtained from our deepest observation of FRB 20200120E with Chandra (Fig. 4). Magnetars hosted in FRB 20200120E's globular cluster would require a different formation channel from those of young magnetars in the Milky Way (for example, via accretion-induced collapse of a white dwarf (WD) or a merger-induced collapse of a WD–WD, NS–WD or NS–NS binary)[43,44]. Since the maximum persistent X-ray luminosities of magnetars formed through core-collapse and delayed channels are predicted to be similar, we would have to probe at least an order of magnitude deeper to reach the level of persistent X-ray emission expected from an extragalactic, FRB-emitting magnetar.

Young extragalactic pulsars

Some models propose that FRBs may be supergiant radio pulses from young, rapidly-rotating extragalactic pulsars[45,46], which may have

similar properties to the Crab pulsar. Several of the radio bursts detected from FRB 20200120E have emission characteristics that are remarkably similar to radio pulses from the Crab pulsar. For example, some radio bursts from FRB 20200120E display multiple pulse components with widths shorter than 100 ns (refs. [21,22]), resembling the nanoshot radio emission observed from the Crab pulsar[47,48]. However, we found no significant evidence of prompt X-ray emission from FRB 20200120E (down to timescales of 100 ns using NICER data) at the times of radio bursts or at other times during our multiwavelength campaign. Our X-ray observations did not have sufficient sensitivity to detect X-ray luminosities comparable to the pulsed X-ray emission from the Crab pulsar (~$0.1 L_X^{Crab}$).

Our persistent X-ray luminosity limits (Fig. 4) show that FRB 20200120E is not associated with a supernova remnant (SNR) or a pulsar wind nebula (PWN) whose persistent X-ray luminosity is larger than or comparable to the Crab Nebula ($L_X^{Crab} \approx 10^{37}$ erg s^{-1}). However, a Crab-like SNR is not expected in FRB 20200120E's ~10-Gyr-old globular cluster since all massive stars that could have produced this type of SNR would have died within the first ~100 Myr of the cluster's formation. Most PWNe have persistent X-ray luminosities of ~0.001–0.01 L_X^{Crab} (refs. [49,50]), which is ~10–100 times below our persistent X-ray luminosity limits and would not have been detectable during our observations.

Millisecond pulsars

FRB 20200120E may be powered by a giant pulse-emitting millisecond pulsar (MSP), spun-up by accretion from a companion star and possibly formed via accretion-induced collapse of a massive WD in a close binary system[51,52]. Globular clusters have high stellar densities and host populations of MSPs that are produced through frequent dynamical interactions. Quasi-periodic microstructure ($P_\mu \approx 2$–3 µs) has been
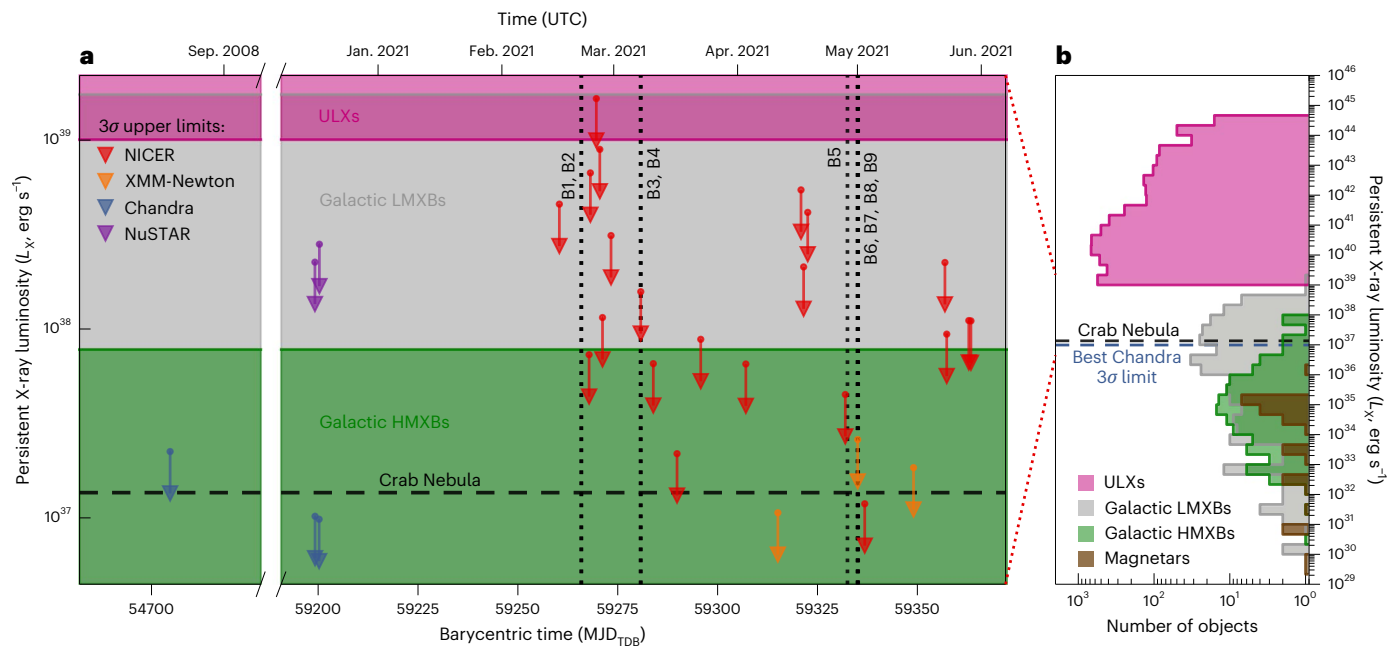
Fig. 4 | Persistent X-ray luminosity limits from observations of FRB 20200120E, compared with the persistent X-ray luminosities of ULX sources, Galactic LMXBs, Galactic HMXBs and magnetars. a, 3σ persistent isotropic-equivalent X-ray luminosity limits from NICER (red), XMM-Newton (orange), Chandra (blue) and NuSTAR (purple) observations of FRB 20200120E. These X-ray luminosity limits are calculated using the 3σ persistent X-ray flux upper limits listed in Extended Data Table 2 and the distance to FRB 20200120E[122]. The luminosity limits from NICER, XMM-Newton and Chandra observations are derived in the 0.5–10 keV energy band, and the luminosity limits from NuSTAR observations are derived in the 3–79 keV energy band. The vertical dotted black lines indicate the barycentric arrival times of the radio bursts shown in

Fig. 1 (Extended Data Table 3). The horizontal dashed black line corresponds to the X-ray luminosity of the Crab Nebula. The shaded pink, grey and green regions indicate the range of X-ray luminosities of ULX sources, Galactic LMXBs and Galactic HMXBs spanning the persistent X-ray luminosity limits from FRB 20200120E. **b**, Histograms showing the persistent X-ray luminosity distributions of ULX sources (pink), Galactic LMXBs (grey), Galactic HMXBs (green) and magnetars (brown). The dashed blue line shows the most constraining 3σ persistent X-ray luminosity limit from a Chandra observation of FRB 20200120E on MJD 59200 (17 December 2020). The dotted red lines indicate the overlapping range of persistent X-ray luminosities from **b** that are shown in **a**.

detected in a radio burst from FRB 20200120E[21], which may indicate that the source is a rapidly spinning pulsar (with a rotational period of $P_{spin} \approx 2$–3 ms) based on the phenomenological P_μ–P_{spin} relationship observed from Galactic pulsars.

Several Galactic MSPs, such as PSR B1937+21 (ref. 53) and PSR B1957+20 (ref. 54), frequently produce giant radio pulses. Some of these giant pulses have nanosecond pulse widths ($w_t < 15$ ns) and high brightness temperatures ($T_b > 5 \times 10^{39}$ K)[53]. In the soft X-ray band, a correlation has been observed between the persistent X-ray luminosity and spin-down luminosity (L_{spin}) of MSPs, that is, $L_X \propto L_{spin}^{1.3}$ (ref. 55). The persistent X-ray luminosities of Galactic MSPs are typically less than 10^{34} erg s^{-1} (ref. 55), which is several orders of magnitude below our deepest persistent X-ray luminosity limits (Fig. 4). This level of persistent X-ray emission, from a putative population of similar MSPs in FRB 20200120E's globular cluster, was not detectable during our observations.

### ULXBs in extragalactic globular clusters
ULXBs are a class of luminous, extragalactic X-ray flares that display fast rise times (~1 min), high peak luminosities (~10^{39}–10^{43} erg s^{-1}) and slow decay timescales (~1 h). Several ULXBs have been identified in nearby galaxies[56–58], but their origins remain unknown. Most sources of ULXBs have been found to be spatially coincident with globular clusters in their host galaxies[56–58]. An association between repeating ULXBs and repeating FRBs has been proposed[59], which is particularly relevant for FRB 20200120E because of its globular cluster location. If X-ray flares similar to ULXBs were produced by FRB 20200120E, their apparent soft X-ray fluences would be at least an order of magnitude larger than our X-ray fluence limits obtained using NICER and XMM-Newton at the times of bursts B4 and B9 (Fig. 5 and Table 1). We conclude that there were no

ULXBs emitted from FRB 20200120E during our X-ray observations, since we did not detect any astrophysical X-ray flares. These observations allow us to rule out a link between FRB 20200120E and ULXBs.

ULX and accretion-powered sources
X-ray binaries, involving accreting NSs or black holes (BHs), have also been proposed as a class of possible FRB sources[60,61], where mass transfer can occur near or exceeding the Eddington rate. ULX sources have persistent X-ray luminosities exceeding 10^{39} erg s^{-1}, some of which have been found to be powered by pulsars in binary systems accreting at super-Eddington rates[62]. The accretion luminosity (L_{acc}) generated by a mass accretion rate, $\dot{M}_{acc}$, is given by $L_{acc} \approx \eta_{acc}\dot{M}_{acc}c^2$, where η_{acc} is the accretion efficiency and c is the speed of light. Assuming that any putative X-ray emission from FRB 20200120E is powered via accretion with an accretion efficiency of $\eta_{acc} = 0.1$, our best persistent X-ray luminosity limit from Chandra observations of FRB 20200120E (Fig. 4 and Extended Data Table 2) corresponds to an upper limit on the mass transfer rate of $\dot{M}_{acc} < 0.06\dot{M}_{Edd}$ for a canonical 1.4 $M_\odot$ NS and $\dot{M}_{acc} < 0.003\dot{M}_{Edd}$ for a 30 $M_\odot$ BH, where $\dot{M}_{Edd}$ is the Eddington accretion rate of the compact object. Our X-ray observations rule out the possibility that FRB 20200120E is associated with an X-ray source accreting persistently at either near-Eddington or super-Eddington levels. Although an intermittently accreting X-ray source cannot be excluded, it is challenging to reconcile our observations with an X-ray system accreting transiently at hyper-Eddington rates ($\dot{M}_{acc} \gtrsim 10\dot{M}_{Edd}$), even for a low-mass (1 $M_\odot$) compact object, since X-ray luminosities ($L_X > 10^{39}$ erg s^{-1}) similar to ULX sources would be required. As shown in Fig. 4a, almost all of our X-ray observations yielded persistent X-ray luminosity limits below 10^{39} erg s^{-1}, which would have been sufficient to detect ULX sources at the location of FRB 20200120E.
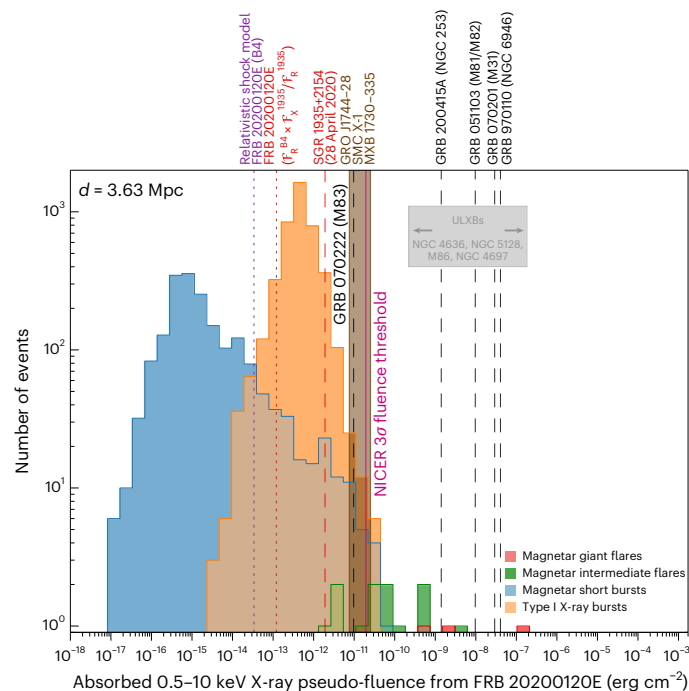
Fig. 5 | Absorbed X-ray pseudo-fluence distributions of X-ray transients from the distance of FRB 20200120E in the 0.5–10 keV energy range, compared with our best prompt X-ray fluence limit from FRB 20200120E. The red, green, blue and orange histograms show the X-ray pseudo-fluence distributions of magnetar giant flares, magnetar intermediate flares, magnetar short bursts and type I X-ray bursts from LMXBs[117], respectively. The vertical magenta line corresponds to our best prompt X-ray fluence limit from FRB 20200120E, derived from NICER observations at the time of burst B4. The X-ray fluence limit derived from XMM-Newton observations at the time of burst B9 is similar to the NICER X-ray fluence limit derived at the time of B4 (Table 1). The NICER X-ray fluence limit is only shown for clarity. The grey rectangle shows the range of X-ray pseudo-fluences derived from ULXBs detected from nearby galaxies[56–58]. The vertical dashed black lines indicate the X-ray pseudo-fluences of GRBs believed to be associated with giant flares from extragalactic magnetars[108–113]. The vertical dashed red line shows the predicted X-ray fluence of the X-ray burst associated with the FRB-like radio burst detected from SGR 1935+2154 on 28 April 2020[12], if it were emitted from the location of FRB 20200120E. The vertical dotted red line indicates the predicted X-ray fluence of burst B4, assuming the same X-ray-to-radio fluence ratio as the FRB-like radio burst detected on 28 April 2020 from SGR 1935+2154 (refs. 8,9,12). The shaded brown region corresponds to the range of X-ray pseudo-fluences derived from bright type II X-ray bursts from GRO J1744–28 (ref. 114) and MXB 1730–335 (ref. 115), and X-ray flares resembling type II X-ray bursts from SMC X-1[116]. The vertical dotted purple line shows the X-ray pseudo-fluence of the flare predicted for burst B4 from FRB 20200120E, based on predictions from the relativistic shock model[26,27] (Methods and Supplementary Information). The X-ray pseudo-fluences were calculated using a distance of $d = 3.63 \pm 0.34$ Mpc (ref. 122) to FRB 20200120E.

The most energetic burst (B4) shown in Fig. 1 has an isotropic-equivalent radio luminosity of approximately 10^{37} erg s^{-1} and a burst duration of roughly 100 μs (Extended Data Table 3). The accretion-based X-ray binary FRB model in ref. 60 predicts mass transfer rates of ~0.1–10 $\dot{M}_{\text{Edd}}$ for radio bursts with durations of 100 μs. A 1.4 $M_\odot$ NS accreting at the Eddington rate ($\dot{M}_{\text{acc}} = \dot{M}_{\text{Edd}}$) would produce an X-ray luminosity of 2×10^{38} erg s^{-1}, which was not detected during most of our X-ray observations. Larger X-ray luminosities would be produced for more massive compact objects as a result of higher Eddington mass transfer rates. X-ray limits from FRBs more distant than FRB 20200120E have excluded ULX sources brighter than $L_X \gtrsim 10^{40}$ erg s^{-1} from being associated with a subset of the FRB population[63]. Our X-ray observations allow us to rule out an association between FRB 20200120E and

ULX/accreting sources with persistent X-ray luminosities larger than $L_X > 9.8 \times 10^{36}$ erg s^{-1}. We also exclude transient, FRB-emitting ULX and accreting sources brighter than $L_X > (1.2–15.8) \times 10^{37}$ erg s^{-1} that are X-ray active when radio emission is produced, based on the X-ray luminosity limits derived near the times of FRB 20200120E's bright radio bursts (Fig. 4a and Extended Data Table 2).

Conclusions

Based on our prompt X-ray fluence limits, we rule out an association between FRB 20200120E and the following types of transient X-ray emission: (1) magnetar giant flares, (2) an SGR 1935+2154-like intermediate flare and (3) ULXBs. Although a significant fraction (~75%) of known intermediate flares from magnetars would have been detectable from FRB 20200120E during our X-ray observations, along with some bright magnetar short bursts and type I and type II X-ray bursts from LMXBs (Supplementary Information), we cannot entirely rule them out as a class.

In addition, our persistent X-ray limits allow us to rule out the following source types for FRB 20200120E: (1) compact objects (for example, young extragalactic pulsars) embedded in an SNR or PWN, with persistent X-ray luminosities larger than or comparable to the Crab Nebula; (2) ULX and accreting sources with persistent X-ray luminosities larger than $L_X > 9.8 \times 10^{36}$ erg s^{-1}; and (3) transient ULX/accreting sources with $L_X > (1.2–15.8) \times 10^{37}$ erg s^{-1} that produce bright, persistent X-ray emission near the times of radio bursts. Although LMXBs with persistent X-ray luminosities comparable to ~30% of the brightest LMXBs in the Milky Way were also detectable from FRB 20200120E's location during our X-ray observations, an LMXB origin for FRB 20200120E cannot be entirely excluded.

A giant radio pulse-emitting pulsar or a magnetar formed through a delayed channel are both potential source types that could explain the physical origin of FRB 20200120E, given its localization to a globular cluster[17]. Deeper X-ray observations in the future, particularly with sensitive, next-generation X-ray instruments, could help further constrain the nature of the astrophysical source powering FRB 20200120E.

Methods

Radio observations

EVN. FRB 20200120E was observed with the 100-m Effelsberg radio telescope during interferometric observations with radio telescopes from the EVN on 20 February 2021; 7, 10, 16 and 22 March 2021; 10 and 28 April 2021; and 2 May 2021. These observations were carried out as part of the PRECISE VLBI programme[17,22]. During each observation, 2-bit sampled dual circular polarization baseband voltage data were recorded between 1,254 and 1,510 MHz in 16 contiguous 16-MHz sub-bands using the Effelsberg radio telescope, which provided a total bandwidth of 256 MHz and a native time resolution of 31.25 ns. These voltage data were saved in VLBI Data Interchange Format (VDIF)[64]. Total intensity filterbank data were also simultaneously recorded using the PSRIX pulsar backend[65] between 1,255 and 1,505 MHz with a time and frequency resolution of 102.4 μs and 0.49 MHz, respectively. These observations are listed in Extended Data Table 1, and additional details are provided in refs. 17,22,66.

A series of simultaneous X-ray observations with NICER and XMM-Newton (Extended Data Fig. 1 and Extended Data Table 2) were performed during all of these PRECISE observing sessions, except for those occurring on 20 February 2021 and 28 April 2021. In total, five radio bursts were detected using the Effelsberg radio telescope during this campaign. Bursts B1 and B2 were detected on 20 February 2021, B3 and B4 were detected on 7 March 2021, and B5 was detected on 28 April 2021. These radio bursts (B1–B5) were discovered by first converting the baseband voltage data from VDIF to filterbank format using digifil[67], with a time and frequency resolution of 64 μs and 125 kHz, respectively. The total intensity filterbank data were then dedispersed using dispersion measure (DM) trials within ±50 pc cm^{-3}

of the expected DM (87.818 pc cm^{-3}), based on radio bursts detected from FRB 20200120E using CHIME/FRB[16]. Candidate radio bursts were identified using a Heimdall-based[68] FRB search pipeline, which were then classified using a deep neural network, available in the Fast Extragalactic Transient Candidate Hunter (FETCH) software package[69]. This burst search pipeline is described in more detail in refs. 17,22,70.

The radio data containing B1–B5 were processed using the Super FX Correlator (SFXC)[71], coherently dedispersed within each 16-MHz subband using a DM of 87.75 pc cm^{-3} and incoherently shifted between the subbands[17,22]. The temporal width and frequency extent of each burst was measured by performing a nonlinear least-squares fit of a two-dimensional Gaussian function to the two-dimensional autocorrelation function of the dynamic spectrum[22]. The peak signal-to-noise ratio (S/N), peak flux density, fluence, isotropic-equivalent luminosity and isotropic-equivalent energy of bursts B1–B5 were determined using dedispersed total intensity data, sampled at 8 μs, and the ±2σ burst width region (Fig. 1 and Extended Data Table 3). Additional details are provided in refs. 17,22. The measured properties of bursts B1–B5 are provided in Extended Data Table 3.

Effelsberg. We carried out additional radio observations of FRB 20200120E using the Effelsberg radio telescope and the central beam of the seven-beam 21-cm receiver[72]. Two radio observations were performed on 16 and 17 December 2020, using the Pulsar Fast Fourier Transform Spectrometer (PFFTS) backend[72] and the Effelsberg Direct Digitization (EDD) backend, during simultaneous X-ray observations of FRB 20200120E with NuSTAR and Chandra (Extended Data Fig. 1 and Extended Data Table 2). Total intensity data were recorded using 512 frequency channels in a digital polyphase filterbank between 1,210 and 1,510 MHz, with a time resolution of 54 μs and a frequency resolution of 0.59 MHz. The Effelsberg observations on 16 and 17 December 2020 were conducted using a preliminary position ($\alpha_{J2000} = 09^h57^m56.40^s$, $\delta_{J2000} = 68°49'04.8''$) for FRB 20200120E, which was derived from baseband voltage data of radio bursts detected by CHIME/FRB. These radio observations are listed in Extended Data Table 1.

Two additional radio observations of FRB 20200120E were performed using Effelsberg in the 1,200–1,600 MHz frequency range with the EDD backend on 30 April 2021 and 14 May 2021. These observations were conducted during simultaneous X-ray observations of FRB 20200120E with XMM-Newton (Extended Data Fig. 1 and Extended Data Table 2). We used a preliminary position ($\alpha_{J2000} = 09^h57^m56.00^s$, $\delta_{J2000} = 68°49'32.0''$) from the EVN for the Effelsberg observations of FRB 20200120E conducted on 30 April 2021 and 14 May 2021. During both of these observations, we recorded channelized, full Stokes data in 512 frequency channels, with a time resolution of 64 μs and a frequency resolution of 0.78125 MHz. Data between 1,210 and 1,510 MHz, coinciding with the bandwidth of the 21-cm receiver, were extracted and used for all of our analyses. A list of these radio observations is provided in Extended Data Table 1.

We searched each of these Effelsberg observations for radio bursts using a custom FRB search pipeline, which utilized the routines provided in the PRESTO pulsar search software package[73]. We did not perform any mitigation of radio frequency interference (RFI), since the band was relatively unaffected by RFI. The data from each of these observations were coherently and incoherently dedispersed using a DM of 87.82 pc cm^{-3} (ref. 16). A single pulse search of the dedispersed data was performed to identify radio bursts at this single DM trial. We searched for radio bursts with temporal widths between 64 μs and 20 ms and saved all candidates with a detection S/N above 5. These candidates were each individually inspected for evidence of radio bursts from FRB 20200120E. Four radio bursts (B6, B7, B8 and B9) were identified during the Effelsberg radio observation conducted on 30 April 2021. No other radio bursts were

detected during the other Effelsberg radio observations described above.

In Extended Data Table 3, we provide measurements of the burst properties of B6, B7, B8 and B9. The properties of these bursts were measured after incoherently dedispersing the data with the S/N-maximizing DM obtained from B9. The DM obtained from B9 was used for dedispersion since it was the brightest and narrowest radio burst detected during the observation. The temporal widths of bursts B6–B9 were determined by fitting a Gaussian function to the dedispersed, frequency-summed burst profiles using a nonlinear least-squares fitting procedure. The burst width is defined as the full-width at half-maximum of the Gaussian fit divided by $\sqrt{2}$. We used the ±2σ burst width region (Fig. 1 and Extended Data Table 3) to determine the peak S/N, peak flux density, fluence, isotropic-equivalent luminosity and isotropic-equivalent energy of bursts B6–B9. Our measurements of the frequency extent of these bursts were obtained from the number of frequency channels displaying a statistically significant 'on-pulse' signal above the noise. The peak flux densities and fluences of bursts B6–B9 were calculated using the radiometer equation and assuming a system equivalent flux density (SEFD) of 15 Jy (ref. 72), since a flux calibrator was not observed.

The fluence detection threshold for a given burst width, w_t, can be calculated using

$$\mathcal{F}_{R,min} = S/N \times \frac{SEFD}{\sqrt{n_p \Delta v}} \times \sqrt{w_t}, \tag{1}$$

where SEFD = T_{sys}/G, T_{sys} is the system temperature, G is the telescope gain, n_p is the number of summed polarizations and Δv is the observing bandwidth. Using equation (1) and assuming a fiducial burst width of 100 μs, we find that the 7σ fluence detection threshold was $\mathcal{F}_{R,min}^{7\sigma} = 0.04$ Jy ms $\sqrt{\frac{w_t}{100\,\mu s}}$ during these Effelsberg observations. We estimate a conservative 15% error on this measurement, based on the uncertainty on the SEFD at the time of these observations.

As part of a radio monitoring programme of FRB 20200120E, additional radio observations were carried out with the Effelsberg telescope on 11, 16 and 18 April 2021 in the 1,233–1,483 MHz frequency range using the PSRIX pulsar backend[65] in baseband mode. During each observation, total intensity filterbank data were recorded with a time and frequency resolution of 65.5 μs and 0.24 MHz, respectively. Dual circular polarization raw voltages were also simultaneously recorded. No radio bursts from FRB 20200120E were detected during these observations. Additional details and results from these radio observations are provided in ref. 66. Coordinated X-ray observations with NICER and XMM-Newton were also performed simultaneously during these Effelsberg observations (Extended Data Fig. 1 and Extended Data Tables 1 and 2).

CHIME. We observed FRB 20200120E in the 400–800 MHz frequency range with the CHIME radio telescope and the CHIME/Pulsar system[74] during multiple simultaneous X-ray exposures with NICER and XMM-Newton (Extended Data Table 2). A list of the radio observations performed using CHIME/Pulsar is provided in Extended Data Table 1. The start times, end times and durations of these observations are displayed in Extended Data Fig. 1. Total intensity data, sampled at 8 bits per sample, were recorded from FRB 20200120E using the CHIME/Pulsar backend. The data from each observation were channelized, coherently dedispersed in real time and saved in a digital polyphase filterbank with 1,024 frequency channels for FRB searches. The CHIME/Pulsar radio observations performed on 15, 24, 26 and 28 February 2021, 11 April 2021 and 1 May 2021 were coherently dedispersed using a DM of 87.78 pc cm^{-3}. A refined DM of 87.757 pc cm^{-3} was used to coherently dedisperse the radio observations carried out on 23 and 29 May 2021.

Before searching the channelized filterbank data for FRBs, the data were reduced using the algorithms described in refs. [7,75–77]. We first masked frequency channels that were known to be regularly contaminated by RFI. The data from each observation were then corrected for the bandpass slope across the frequency band. Next, we removed low-frequency temporal variations from the channelized data by subtracting the moving average from each data value in each frequency channel, which was calculated using a sliding window spanning 0.5 s around each time sample. The data in each frequency channel were then rescaled to have a mean of zero and a standard deviation of one. To further mitigate narrowband and wideband RFI, we used the rfifind routine, available in the PRESTO pulsar search software package[73], to generate a mask that was applied to excise additional data corrupted by RFI.

To search for radio bursts from FRB 20200120E, the filterbank data from each observation were incoherently dedispersed with DMs between 87.70 and 87.90 pc cm^{-3} using 201 DM trials, with $\Delta DM_{trial} = 0.001$ pc cm^{-3}. FRB candidates were identified by convolving each dedispersed time series with boxcar functions, with logarithmically-spaced widths between the time resolution of each observation and 100 ms, using a Fourier-domain matched-filtering algorithm. The detection S/N of each candidate was calculated using

$$S/N = \frac{\sum_i (f_i - \bar{\mu})}{\bar{\sigma}\sqrt{w_b}}, \qquad (2)$$

where f_i is the value of the time series at the ith bin of the boxcar function, $\bar{\mu}$ and $\bar{\sigma}$ are the local mean and root mean square (RMS) noise after normalization, and w_b is the boxcar width in number of bins. Before calculating the detection S/N of each candidate, the dedispersed, frequency-summed data were detrended and normalized so that $\bar{\mu} \approx 0$ and $\bar{\sigma} \approx 1$. Candidates with S/N ≥ 7 from each DM trial were recorded and visually inspected to determine if the event was astrophysical. No radio bursts were detected from FRB 20200120E during our observations with CHIME/Pulsar.

The SEFD was approximately 23 Jy during these CHIME/Pulsar observations[74]. Using equation (1), we place 7σ upper limits of $\mathcal{F}_{R,min}^{7\sigma} < 0.06$ Jy ms $\sqrt{\frac{w_t}{100\,\mu s}}$ on the fluence of radio bursts from FRB 20200120E in the 400–800 MHz band during the times of our radio observations with the CHIME/Pulsar system, assuming a fiducial burst width of $w_t = 100$ μs. However, we note that the data from our CHIME/Pulsar observations on 20, 24, 26 and 28 February 2021 were recorded using a time resolution of 327.68 μs (Extended Data Table 1), making them suboptimal for detecting radio bursts with widths smaller than the sampling time. We estimate a conservative 50% error on these radio fluence limits, based on the uncertainty on the SEFD during these radio observations with the CHIME/Pulsar system.

X-ray observations

NICER. NICER is an X-ray telescope operating on the International Space Station[78,79]. The X-ray Timing Instrument (XTI) is the primary instrument onboard NICER, which is composed of 56 co-aligned cameras (52 operational on orbit) that are sensitive to detecting photons in the 0.2–15 keV energy band[80]. Each camera contains an X-ray concentrator and a non-imaging silicon drift detector, which is referred to as a Focal Plane Module (FPM)[81]. The FPMs are arranged in a 7 × 8 array and provide a field of view of roughly 30 arcmin^2. X-ray photons detected by the XTI are time-tagged with an absolute accuracy, relative to Global Positioning System (GPS) time, of better than 100 ns (RMS), and the photon energies are measured to a precision of ~2% (ref. [82]). The nominal effective area of the XTI, combining all operational detectors, is 1,840 cm^2 at 1.5 keV.

We performed observations of FRB 20200120E with NICER in the 0.2–15 keV energy band between 15 February 2021 and 30 May 2021. A list of these NICER observations is provided in Extended Data Table 2,

and a timeline of these observations is shown in Extended Data Fig. 1. These NICER observations were each processed using the FTOOLS[83] and HEASoft[84] (version 6.31.1) software packages, along with the NICER Data Analysis Software (nicerdas; version 10.0, 2022-12-16_V010a) and NICER calibration database (CALDB; version xti20221001). Cleaned event files were produced from the raw data using the nicerl2 processing pipeline, which applies 'Level2' calibration and performs data screening. The nicerl2 pipeline executes five primary subtasks: (1) nicercal (applies the standard NICER calibration to each observation), (2) niprefilter2 (creates augmented 'Level2' filter files for filtering data and generating background estimates), (3) nimaketime (generates a Good Time Interval (GTI) file for event screening), (4) nicermergeclean (combines NICER data from independent Measurement Power Unit slices (MPUs) and applies screening criteria to the data) and (5) niautoscreen (performs additional screening of FPMs and MPUs to exclude bad data from detectors and time ranges that may have been missed by the screening applied by the nimaketime routine).

Standard screening criteria were used to generate the cleaned event files. We selected data during time intervals when the angular distance between FRB 20200120E and NICER's boresight was <54″, the elevation angle was >30° with respect to the bright Earth limb, and NICER was outside of the South Atlantic Anomaly. The underonly_range parameter, which is used to screen for high optical loading, was set to '0–500'. The overonly_range parameter, which is used to mitigate high particle background, was set to '0–30'. We selected photons in the 0.5–10 keV energy range for most of our analyses. Cleaned event files were also generated in the 0.4–4 keV and 0.2–15 keV energy bands for X-ray burst and pulsation searches.

We excluded data from two FPMs (DET_IDs 14 and 34), since they have been observed to display episodes of increased detector noise. We also excluded X-ray photons from 'hot' detectors, which were determined for each Observation ID by identifying detectors whose photon counts were more than 3σ above the mean number of photons, calculated using all of the 'good' detectors. The set of 'good' detectors was determined for each Observation ID as FPMs whose behaviour was not significantly different from the detector group.

The photon arrival times in each cleaned event file were corrected to the Solar System barycentre using the barycorr tool, the Jet Propulsion Laboratory (JPL) DE405 ephemeris, and the position of FRB 20200120E determined from VLBI with the EVN[17]. The photon times were determined using the Barycentric Dynamical Time (TDB) system. After barycentring, the relative accuracy of the NICER photon timestamps is ~80 ns.

XMM-Newton. Observations of FRB 20200120E were performed using XMM-Newton on 10–11 April 2021 (Observation ID 0872392401), 30 April to 1 May 2021 (Observation ID 0872392501) and 14–15 May 2021 (Observation ID 0872392601). These observations (Extended Data Fig. 1 and Extended Data Table 2) were targeted at FRB 20200120E using a preliminary position ($\alpha_{J2000} = 09^h57^m56.00^s$, $\delta_{J2000} = 68°49'32.0''$) determined using the EVN. The EPIC/MOS and EPIC/pn detectors were operated in Large Window mode, providing time resolutions of 0.9 s and 47.7 ms, respectively. We opted to use Large Window mode during these XMM-Newton observations, instead of Timing mode, because it provided a lower background level with spatial information and high live time.

The XMM-Newton data were reduced and analysed using standard tools from the XMM-Newton Science Analysis System (XMM-SAS; version 19.1.0)[85] and HEASoft[84] (version 6.28) software packages. Standard filters were applied to retain good events in the 0.5–10 keV energy band from the EPIC/MOS and EPIC/pn detectors. The XMM-Newton EPIC/pn X-ray photons were extracted using a point-spread function (PSF) centred on FRB 20200120E's position from VLBI[17]. Source events were extracted from a circular region of radius 18″, centred on the source position, and background events were extracted from an annular region

with an inner diameter of 18″ and outer diameter of 72″. The photon event arrival times were corrected to the Solar System barycentre using the VLBI-determined position of FRB 20200120E[17].

Chandra. We observed FRB 20200120E using Chandra on 16 and 17 December 2020 (Observation IDs 23544 and 24894), using the High Resolution Camera (HRC) in Timing mode (Extended Data Fig. 1 and Extended Data Table 2). This mode provides a time resolution of 16 μs (ref. 86). We selected this mode because FRB 20200120E was localized to only arcminute precision[16] at the time, and thus, a large field of view and high time resolution were required at the expense of effective area. These Chandra observations of FRB 20200120E were targeted at a preliminary position ($\alpha_{J2000} = 09^h57^m56.40^s, \delta_{J2000} = 68°49'04.8''$), derived using baseband voltage data from CHIME/FRB. We also analysed an archival Chandra ACIS observation from 24 August 2008 (Observation ID 9540), previously presented in ref. 17, where FRB 20200120E was located 14′ from boresight.

We used the Chandra Interactive Analysis of Observations (CIAO; version 4.12) software package[87] and standard procedures to reduce and analyse the Chandra observations. For the HRC observations, source photons were extracted from a circular region of radius 1″, centred on the VLBI position of FRB 20200120E[17]. Since FRB 20200120E was located 14′ off-axis in Observation ID 9540, events were extracted from a 10″-radius region at the position of FRB 20200120E, and background events were extracted from a 60″-radius region at a similar off-axis angle. The photon event arrival times were then corrected to the Solar System barycentre.

NuSTAR. NuSTAR observations of FRB 20200120E (Extended Data Fig. 1 and Extended Data Table 2) were performed nearly simultaneously with the Chandra observations on 16 and 17 December 2021 (Observation IDs 80701506002 and 80701506004). The data were reduced using the standard nupipeline and nuproducts routines available in the HEA-Soft (version 6.28) software package. We corrected the photon arrival times to the Solar System barycentre using the barycorr tool. Source events were extracted from a circular region of radius 2′, centred on the position of FRB 20200120E determined from VLBI[17]. Background events were extracted from a region of the same size positioned away from the source.

X-ray burst searches and prompt X-ray fluence limits
NICER. We carried out a blind search for X-ray bursts during each of the NICER observations of FRB 20200120E listed in Extended Data Table 2. We independently searched for X-ray bursts using the unbinned photon event times during GTIs in three different energy ranges: 0.4–4 keV, 0.5–10 keV and 0.2–15 keV. These energy bands were chosen to maximize the sensitivity to detecting X-ray bursts, both within the most sensitive part of NICER's photon energy bandpass and over a broader range of photon energies.

We used a Bayesian Blocks technique[88] to search for X-ray bursts with durations up to 100 s during each NICER Observation ID. Bayesian Blocks is a dynamic programming algorithm that determines the optimal segmentation of the data and an optimal histogram characterizing the data with adaptive bin widths. This algorithm can detect and characterize statistically significant variations using event data, binned data or measurements at arbitrary times with known error distributions, and it is not limited by signal amplitude, time resolution or sampling of the data. In the Bayesian Blocks algorithm, the optimal block partition is obtained by maximizing the likelihood function ($\mathcal{L}$)[88] using

$$\ln \mathcal{L}_k = N_k \ln \lambda_k - \lambda_k T_k, \qquad (3)$$

where N_k is the number of events in block k, T_k is the length of block k, and $\lambda_k = N_k/T_k$ is the expected count rate in block k. The following prior

distribution (ncp_prior)[88] for the number of blocks was used when the Bayesian Blocks algorithm was applied to the unbinned NICER event data from FRB 20200120E:

$$\text{ncp\_prior} = 4 - \ln(73.53 p_0 N^{-0.478}), \qquad (4)$$

where N is the total number of events, and we have chosen $p_0 = 0.05$ for the false positive probability.

The detection significance of each candidate burst was determined by calculating the Poisson probability of detecting the observed number of photons in the block, given a non-burst count rate estimated from nearby 1 s time intervals. In all cases, no X-ray bursts were detected above a 3σ probability detection threshold, corresponding to a false alarm probability (P_{fa}) of $P_{fa} < 0.0027$.

XMM-Newton, Chandra and NuSTAR. Several radio bursts (B6–B9) were detected from FRB 20200120E using the Effelsberg radio telescope during the XMM-Newton observations performed between 31 April and 1 May 2021 (Observation ID 087238501) (Extended Data Fig. 1). Unfortunately, these observations were contaminated by soft proton flares, so we only consider the last radio burst (B9) detected using Effelsberg, which occurred at a time when the contamination was low. We searched for X-ray bursts near the time of burst B9 by considering the nearest photons, detected using XMM-Newton's EPIC/pn camera, to the barycentric ToA of the radio burst at infinite frequency. The nearest photon occurred 58.4 s before burst B9 (Extended Data Fig. 4e). Based on the count rate measured from the background region, the false alarm probability of a photon arriving in such a time window is $P_{fa} = 0.33$. We also considered the ten nearest photons from the ToA of B9 to probe for X-ray bursts on longer timescales (up to ~600 s). For time windows spanning the second to tenth nearest photons to B9, there was no statistically significant X-ray emission above a 3σ probability detection threshold ($P_{fa} < 0.0027$). We repeated this search using data from the EPIC/MOS1 and EPIC/MOS2 cameras, and we also found no statistically significant X-ray excess above a 3σ probability detection threshold ($P_{fa} < 0.0027$).

In addition, we carried out searches for X-ray bursts at all times during the XMM-Newton observations by searching for excesses from the Poisson background rate on 0.1 s, 1 s, 10 s and 100 s timescales, where the minimum search timescale was set by the 47.7 ms time resolution of the XMM-Newton EPIC/pn data. We searched for evidence of enhanced X-ray emission by comparing the binned light curves of the source and background regions. After taking into account the number of search trials, no bins in the source light curves exceeded a 3σ probability detection threshold ($P_{fa} < 0.0027$).

We performed a blind search for X-ray bursts at all times during the Chandra and NuSTAR observations of FRB 20200120E. Following the same search procedure as described above for the XMM-Newton EPIC/pn data, we searched for statistically significant deviations from the background rate on 0.1 s, 1 s, 10 s and 100 s timescales. However, since the background count rate did not show any significant variability, we compared with a single background rate derived from the entire observation, instead of using a binned background light curve. No statistically significant excess X-ray emission was found above a 3σ probability detection threshold ($P_{fa} < 0.0027$) at any of these timescales.

Prompt X-ray fluence limits. We used the Bayesian method described in ref. 89 to derive X-ray fluence limits at the times of bursts B4 and B9. Using the number of detected photons and the expected number of background photons, we obtained standard 3σ confidence intervals describing the number of observed photons on a variety of timescales. Confidence intervals were calculated for burst B4 on timescales of 100 ns to 10 s using measurements from NICER and on timescales of 100 ms to 100 s using measurements from XMM-Newton's EPIC/pn camera for burst B9. These confidence intervals were then translated

into an X-ray fluence limit for each spectral model listed in Table 1. For burst B4, we report the most conservative limit after considering each of the NICER background estimates listed in Extended Data Table 4. Background estimates for burst B9 were derived from the background count rate measured using XMM-Newton's EPIC/pn camera.

Sensitivity to detecting short X-ray bursts with NICER. To characterize NICER's nominal sensitivity to detecting short X-ray bursts with temporal widths between 100 ns and 10 s, we performed an analysis of observations of six blank sky regions that are free of detectable X-ray point sources. The observations used in this analysis are labelled 'BKGD_RXTE_B_i', where B_i = {1, 2, 3, 4, 5, 6, 8}. These fields are routinely observed by NICER, and they were previously used by the Rossi X-ray Timing Explorer (RXTE) for background modelling[90]. We note that one of these background fields, 'BKGD_RXTE_6' ($\alpha_{J2000} = 10^h 40^m 00^s$, $\delta_{J2000} = 72°34'12'$), is only ~5° offset from the VLBI position of FRB 20200120E[17]. Observations of 'BKGD_RXTE_7' were not used in our analysis because a bright, soft X-ray-emitting star is located in the field. These data can be accessed through NASA's High Energy Astrophysics Science Archive Research Center (HEASARC) archive. We used these observations to empirically measure NICER's detector and sky background on short timescales.

We processed all of the available NICER blank sky observations ('BKGD_RXTE_B_i') performed between 25 June 2017 and 6 February 2022 using the nicerl2 pipeline with standard calibration and data screening parameters. X-ray photons in the 0.5–10 keV energy range were selected for our background analysis. We excluded photons from two active FPMs (DET_IDs 14 and 34) that are known to exhibit episodes of increased detector noise. We also excluded X-ray photons from 'hot' detectors from each exposure, using the method described above (see X-ray observations). We included all exposures with GTIs spanning at least 200 s in our analysis. Using standard parameters, the nicerl2 pipeline was unable to completely remove all of the contamination from some of the blank sky exposures near the boundaries of the GTIs. To mitigate this problem, we removed photons from each exposure with arrival times occurring within 1 min of the GTI start and end times. In addition, a small fraction (~3%) of the background observations needed to be excluded due to missing data or poor data quality. After filtering, our analysis included blank sky data from 4,265 independent exposures (total exposure time of 2 Ms), obtained from 1,658 NICER Observation IDs.

The background count rate distribution was modelled separately for each blank sky region using a Bayesian Markov chain Monte Carlo (MCMC) parameter estimation procedure. We generated light curves using data from each background exposure, binned at each of the following time resolutions: 100 ns, 1 μs, 10 μs, 100 μs, 1 ms, 10 ms, 100 ms, 1 s and 10 s. For each background field, we measured the distribution of count rates at each of the above-mentioned time resolutions and then carried out an unbinned likelihood analysis to measure the mean background count rate. Posterior probability distributions for the mean background count rate, λ_b, at each timescale were calculated from MCMC analyses, where we used an uninformed, flat prior for λ_b and a Poisson likelihood function, $\mathcal{L}(\lambda_b | b_i)$, given by

$$\ln \mathcal{L}(\lambda_b | b_i) = -N_b \lambda_b + \ln(\lambda_b) \sum_{i=1}^{N_b} b_i - \sum_{i=1}^{N_b} \ln(b_i!). \quad (5)$$

Here, b_i represents the measured background count rate in each time bin, and the number of background count rate measurements is denoted by N_b.

The posterior probability density functions were sampled using an affine-invariant MCMC ensemble sampler[91], implemented in the emcee software package[92]. The parameter spaces were explored using 200 walkers and a chain length of 5,000 steps per walker. The walkers were initialized to start from a small Gaussian ball centred around

the maximum likelihood estimator. The first 100 steps in each chain were treated as the initial burn-in phase and were removed from the analysis. The posterior probability distributions were calculated using the remaining 4,900 steps in each chain. Best-fit values for the mean background count rate, λ_b, were obtained at each timescale for each blank sky region from the median of the posterior distributions, along with 1σ uncertainties derived from Bayesian credible intervals.

We used these measurements to calculate a single value for λ_b at each timescale from the weighted average of the mean background count rates from all of the blank sky regions. The weighted average values of λ_b were treated as the nominal background rate at each timescale when calculating confidence intervals describing the number of X-ray counts near the times of radio bursts from FRB 20200120E, using the Bayesian method described in ref. 89. In Extended Data Fig. 3a, we show the average, absorbed X-ray background flux of NICER in the 0.5–10 keV energy band for integration times between 100 ns and 10 s using these background count rates, assuming $N_H = 6.73 \times 10^{20}$ cm^{-2} (the Galactic hydrogen column density contribution along the line of sight to FRB 20200120E[24]) and an X-ray spectrum with a photon index of $\Gamma = 1.4$ (similar to the diffuse X-ray background[93]). The corresponding X-ray fluences are shown in Extended Data Fig. 3b on timescales of 100 ns to 10 s.

We compare these results with two independent methods used to estimate the NICER background near the time of burst B4. First, we consider the 'Space Weather' background model[90], which uses a combination of the cut-off rigidity (COR_SAX)[94] and the planetary K-index (K_p)[95] to obtain an estimate of the space weather environment. This model also uses the SUN_ANGLE parameter to account for the low-energy background produced by optical loading. On timescales of 100 ns to 10 s, we find that the predicted NICER background in the 0.5–10 keV energy range from our analysis of blank sky regions is larger and more conservative than the background estimates obtained from the NICER 'Space Weather' model near the time of burst B4[90] (Extended Data Table 4). These measurements are also more conservative than our background estimates obtained from NICER using photons within ±100 s of burst B4 (Extended Data Table 4).

Spectral analysis and persistent X-ray emission

Chandra, NuSTAR and XMM-Newton. For all of the Chandra, NuSTAR and XMM-Newton observations listed in Extended Data Table 2, the number of counts in the source extraction regions was consistent with the background count rate. To place limits on the count rate of a putative X-ray source coincident with FRB 20200120E, we used the Bayesian method described in ref. 89. We then translated the count rate limit to a flux limit by assuming a photoelectrically absorbed power-law source spectrum, with a photon index of $\Gamma = 2$ and a hydrogen column density of $N_H = 6.73 \times 10^{20}$ cm^{-2} towards FRB 20200120E[24], while also accounting for the spectral response of the source. The spectral response was derived using CIAO's specextract tool for the Chandra observations, the nuproducts routine in the HEASoft software package for the NuSTAR observations, and XMM-SAS's arfgen tool for the XMM-Newton observations. In Extended Data Table 2, we list 3σ upper limits on the persistent X-ray flux, derived using this method, in the 0.5–10 keV energy band for each Chandra and XMM-Newton observation, and in the 3–79 keV energy band for each NuSTAR observation.

NICER. After the data from each NICER Observation ID (Extended Data Table 2) were processed with the FTOOLS[83] and HEASoft (version 6.31.1) software packages[84], using the nicerl2 standard calibration and filtering pipeline, we used the nicerl3-spect spectral product pipeline to produce source and background spectra, along with ancillary response files (ARFs) and response matrix files (RMFs), for each observation. Background spectra were generated using three different models: (1) an empirical '3C50' background model[90], which can be produced using the nibackgen3C50 FTOOLS routine[90]; (2) the 'SCORPEON' background

model, which is available through the niscorpeon FTOOLS routine and allows the background to be fit as a parameterized model simultaneously with the data; and (3) the 'Space Weather' background model, which is implemented in the niswbkgspect FTOOLS routine. The niswbkgspect routine estimates the space weather conditions during a given observation and produces a NICER background spectrum based on blank sky data matching these conditions. Each of the spectra was optimally rebinned, as described in ref. 96, with a minimum of ten counts per bin using the ftgrouppha FTOOLS routine.

We obtained source and background spectra from each NICER observation in the 0.5–10 keV energy range using each of the background models described above. All of the NICER observations yielded background-dominated spectra, based on comparisons with background spectra generated using these background models. The source spectra from Observation IDs 3658040103, 3658040104 and 3658040105 were marginally inconsistent with the background spectra. However, for these Observation IDs, we attribute this to incompleteness in modelling the time-variable background using the currently available background models. In Extended Data Table 2, we provide 3σ limits on the 0.5–10 keV persistent X-ray flux of FRB 20200120E during each NICER observation, since we did not find evidence of significant persistent X-ray emission.

The 3σ persistent X-ray flux limits from each NICER observation were derived based on a fiducial photoelectrically absorbed power-law spectral model, with a hydrogen column density of $N_H = 6.73 \times 10^{20}$ cm^{-2} (ref. 24) and a photon index of $\Gamma = 2$. For each Observation ID, we used the fakeit routine in the XSPEC (version 12.13.0c) spectral fitting software package[25] to generate simulated spectra using the tbabs(po) spectral model. Simulated spectra for each NICER observation were constructed using the source spectrum, a background spectrum produced using the '3C50' background model, and the ARF and RMF from each observation. The hydrogen column density and photon index were fixed to the above values, and a wide range of trial normalizations were used to produce multiple simulated spectra for each observation. The simulated spectra from each observation were then fit using the source spectrum as an empirical background model, while using the ARF and RMF from each observation. During the fitting process, the hydrogen column density and photon index were fixed, and the normalization was left as a free parameter. The flux routine in XSPEC was used to determine the largest normalization parameter value that yielded a 3σ confidence interval for the 0.5–10 keV X-ray flux that was consistent with non-detection. The 3σ persistent X-ray flux limit on FRB 20200120E during each NICER observation was obtained using the tbabs(po) spectral model, with this normalization parameter value, $N_H = 6.73 \times 10^{20}$ cm^{-2} (ref. 24), and $\Gamma = 2$. The 3σ persistent X-ray luminosity limits shown in Fig. 4 for FRB 20200120E were calculated using the 3σ persistent X-ray flux limits listed in Extended Data Table 2 and the distance to FRB 20200120E.

Periodicity searches

X-ray pulsations. We carried out several independent searches for X-ray pulsations using the NICER data. Each of our analyses was repeated after selecting photons in three different energy bands: 0.4–4 keV, 0.5–10 keV and 0.2–15 keV. These energy ranges were chosen to maximize the sensitivity to detecting X-ray pulsations, both using photons in the most sensitive part of NICER's photon energy bandpass and over a broader range of photon energies.

First, we used all of the NICER observations in Extended Data Table 2 to generate evenly sampled light curves, sampled at 65.536 kHz (time resolution of ~15.3 μs), using X-ray photon arrival times that were corrected to the Solar System barycentre using the position of FRB 20200120E determined from VLBI[17]. These light curves spanned a total duration of 8.94 Ms (103.5 days) and contained ~5.9×10^{11} time bins. We calculated power spectra from fast Fourier transforms (FFTs) of each light curve, which were searched for X-ray pulsations. No astrophysical

candidates were found above a 3σ detection threshold, after accounting for the number of independent frequency trials.

Next, we repeated the search described above using separate light curves derived from NICER observations between: (1) 22 February 2021 and 29 February 2021 (Observation IDs: 3658040102, 3658040103, 3658040104, 3658040105, 3658040106 and 3658040107) and (2) 22 May 2021 and 30 May 2021 (Observation IDs: 3658040109, 3658040110, 3658040111 and 3658040112). These time periods were chosen because they correspond to time intervals when NICER was used to perform X-ray observations of FRB 20200120E with both the highest cadence and largest cumulative exposure over an approximately 1 week period. Searches for X-ray pulsations in these shorter combined datasets provide greater sensitivity to detecting periodicities that may be smeared in the power spectrum of the full light curve spanning 103.5 days, for example, if FRB 20200120E harbours a rotating NS that exhibits changes in its rotational frequency over time. We did not detect any periodic signals above a significance threshold of 3σ in the power spectra derived from these light curves spanning ~1 week.

We also performed 'semi-coherent' searches for X-ray pulsations using power spectra computed from the light curves of each NICER Observation ID. The light curves from each Observation ID were evenly sampled at a time resolution of ~15.3 μs and zero-padded to have the same length as the light curve from Observation ID 3658040105, which spanned the longest duration. This yielded a power spectrum from each NICER Observation ID with the same frequency resolution. The powers in each spectral bin of the power spectra were summed to create a stacked power spectrum, which was then searched for statistically significant peaks. We refer to this technique as a 'semi-coherent' method since powers are added, instead of complex amplitudes, and the overall phase information of the signal between observations is not incorporated. The power spectra used in this analysis were computed from an FFT and also using the Rayleigh statistic[97], Z_n^2, via

$$Z_n^2 = \frac{2}{N} \sum_{k=1}^{n} \left[\left(\sum_{j=1}^{N} \cos k\phi_j \right)^2 + \left(\sum_{j=1}^{N} \sin k\phi_j \right)^2 \right], \quad (6)$$

where n denotes the number of harmonics summed, N is the number of photon ToAs, and ϕ_j is the phase of each ToA calculated at a trial frequency, ν. We used $n = 1$ to derive stacked power spectra with the Z_1^2 statistic. No statistically significant signals were detected above a 3σ detection threshold in the stacked power spectra obtained using the FFT and Z_1^2 statistics.

Assuming a pulsar-like FRB source, we place 3σ limits on FRB 20200120E's pulsed X-ray flux (F_X^{pulsed}). For a duty cycle of 10%, the 3σ upper limits on the pulsed X-ray flux are given by $F_X^{pulsed} = \sqrt{\delta_{PSR}/(1 - \delta_{PSR})}F_X < 0.33F_X$, where δ_{PSR} is the assumed duty cycle of the putative pulsar-like FRB source and F_X is the persistent X-ray flux limit derived at the time of each NICER observation (Extended Data Table 2). The 3σ limits on FRB 20200120E's pulsed X-ray flux range between 2.5×10^{-15} and 3.5×10^{-13} erg cm^{-2} s^{-1} at the times of our NICER observations.

Comparisons with X-ray sources and transients

Persistent X-ray luminosity. In Fig. 4, we compare our persistent X-ray luminosity limits for FRB 20200120E, from Chandra, NICER, NuSTAR and XMM-Newton observations, to the persistent X-ray luminosities of ULX sources, Galactic LMXBs, Galactic HMXBs and magnetars. In each case, we calculated the X-ray luminosity (L_X) from the X-ray flux (F_X) using $L_X = 4\pi d_L^2 F_X/(1 + z)$, where d_L is the luminosity distance of each object and z is the corresponding redshift. Redshifts were determined for each source using the Planck18 routine in the astropy.cosmology Python software package[98], which uses the cosmological parameters measured in ref. 99.

The histogram of persistent X-ray luminosities for ULX sources was calculated using values from the ULX source catalogue available

in ref. 100. We adopt a typical luminosity definition of $L_X \geq 10^{39}$ erg s^{-1} for ULX sources[100,101]. In the pink histogram shown in Fig. 4b, we only included objects from the ULX catalogue with an X-ray luminosity above this threshold. We also only included ULX sources whose luminosity measurement was significant, with respect to its uncertainty. We further selected only ULX sources that were associated with a single potential host galaxy to mitigate contamination from unreliable distance measurements. The persistent X-ray luminosity values were calculated in the 0.2–12 keV energy band, using the 0.2–12 keV X-ray flux of each object and the host galaxy luminosity distances listed in the ULX catalogue.

The grey histogram in Fig. 4b shows the persistent X-ray luminosities of Galactic LMXBs, obtained from measurements provided in the Galactic LMXB catalogue available in ref. 102. We calculated X-ray luminosities in the 0.2–12 keV energy range using the maximum 0.2–12 keV X-ray flux of each source and the average distance listed for each object in the LMXB catalogue. Similarly, the green histogram in Fig. 4b shows the persistent X-ray luminosities of Galactic HMXBs, derived using measurements from the Galactic HMXB catalogue provided in ref. 103. The X-ray luminosities were also calculated in the 0.2–12 keV energy band using the maximum 0.2–12 keV X-ray flux of each source and the average distance listed for each object in the HMXB catalogue. We excluded LMXB and HMXB sources that were missing either a maximum X-ray flux value or a distance value in their respective catalogue. Since maximum X-ray flux values were used to generate these histograms, the grey and green histograms in Fig. 4b show the distributions of Galactic LMXBs and HMXBs in their high X-ray state.

The brown histogram in Fig. 4b shows the distribution of persistent X-ray luminosities for magnetars. We used the unabsorbed X-ray flux values in 2–10 keV energy band and the distance measurements listed in the McGill Magnetar Catalog[39] to calculate an X-ray luminosity for each magnetar. We also included X-ray luminosities from several recently discovered magnetars[34,104–107], determined by translating the reported persistent X-ray flux to the 2–10 keV energy band using the XSPEC spectral fitting software package[25] and the best-fit spectral parameters describing the persistent X-ray emission for each source.

Prompt X-ray pseudo-fluence. The X-ray pseudo-fluence distributions of magnetar giant flares, magnetar intermediate flares, magnetar short bursts and type I X-ray bursts from Galactic LMXBs are shown in Fig. 5. We also show X-ray pseudo-fluence values for GRBs from extragalactic magnetar giant flares, ULXBs from an unknown class of astrophysical sources in extragalactic globular clusters, bright type II X-ray bursts from Galactic LMXBs and predictions from the relativistic shock model in refs. 26,27 (Supplementary Information). The X-ray pseudo-fluence value for each flare or burst was determined by correcting the observed or predicted X-ray fluence for the distance to FRB 20200120E, the expected hydrogen column density towards FRB 20200120E ($N_H = 6.73 \times 10^{20}$ cm^{-2} (ref. 24)), and the best-fit spectral model reported for each event. We calculated X-ray pseudo-fluences in the 0.5–10 keV energy band using the XSPEC spectral fitting software package[25].

The absorbed 0.5–10 keV X-ray pseudo-fluences of magnetar flares and magnetar bursts were determined using values reported in the literature for each event (for example, see refs. 31,36,38). The corresponding values for GRBs from extragalactic magnetar giant flares[108–113], ULXBs[56–58] and bright type II X-ray bursts[114–116] were obtained similarly. The absorbed X-ray pseudo-fluence distribution of type I X-ray bursts was derived from the type I X-ray burst Multi-INstrument Burst ARchive (MINBAR) catalogue[117], using the best-fit blackbody temperature (kT) at burst peak.

Predictions from relativistic shock model

Following the formalism described in ref. 27, we calculate the predicted Lorentz factor of the shocked gas (Γ_{shock}), shock radius (R_{shock}), upstream

external density at the shock radius ($n_{ext}(R_{shock})$) and energy of the relativistic flare (E_{flare}) using the measured duration (w_t) and energy (E_R) of burst B4 from FRB 20200120E (Extended Data Table 3) as follows:

$$\Gamma_{shock} \approx 51 \left(\frac{m_*}{m_e}\right)^{1/30} \left(\frac{f_e}{0.5}\right)^{1/15} \left(\frac{f_\xi}{10^{-3}}\right)^{-1/15} \left(\frac{v_{centre}}{1{,}382\,MHz}\right)^{-7/30}$$
$$\times \left(\frac{w_t}{117\,\mu s}\right)^{-2/5} \left(\frac{E_R}{2.8 \times 10^{33}\,erg}\right)^{1/6} \tag{7}$$

$$R_{shock} \approx 2\Gamma^2 c w_t \approx 1.8 \times 10^{10}\,cm \left(\frac{m_*}{m_e}\right)^{1/15} \left(\frac{f_e}{0.5}\right)^{2/15} \left(\frac{f_\xi}{10^{-3}}\right)^{-2/15}$$
$$\times \left(\frac{v_{centre}}{1{,}382\,MHz}\right)^{-7/15} \left(\frac{w_t}{117\,\mu s}\right)^{1/5} \left(\frac{E_R}{2.8 \times 10^{33}\,erg}\right)^{1/3} \tag{8}$$

$$n_{ext}(R_{shock}) \approx 9.0 \times 10^4\,cm^{-3} \left(\frac{m_*}{m_e}\right)^{2/15} \left(\frac{f_e}{0.5}\right)^{-11/15} \left(\frac{f_\xi}{10^{-3}}\right)^{-4/15}$$
$$\times \left(\frac{v_{centre}}{1{,}382\,MHz}\right)^{31/15} \left(\frac{w_t}{117\,\mu s}\right)^{2/5} \left(\frac{E_R}{2.8 \times 10^{33}\,erg}\right)^{-1/3} \tag{9}$$

$$E_{flare} \approx 5.3 \times 10^{37}\,erg \left(\frac{m_*}{m_e}\right)^{2/5} \left(\frac{f_e}{0.5}\right)^{-1/5} \left(\frac{f_\xi}{10^{-3}}\right)^{-4/5}$$
$$\times \left(\frac{v_{centre}}{1{,}382\,MHz}\right)^{1/5} \left(\frac{w_t}{117\,\mu s}\right)^{1/5} \left(\frac{E_R}{2.8 \times 10^{33}\,erg}\right)^{1/5}. \tag{10}$$

From equation (10), the ratio of the relativistic flare energy to radio burst energy is given by

$$\eta_{shock} = \frac{E_{flare}}{E_R} = \frac{\mathcal{F}_{flare}}{\mathcal{F}_R} \approx 1.9 \times 10^4 \left(\frac{m_*}{m_e}\right)^{2/5} \left(\frac{f_e}{0.5}\right)^{-1/5} \left(\frac{f_\xi}{10^{-3}}\right)^{-4/5}$$
$$\times \left(\frac{v_{centre}}{1{,}382\,MHz}\right)^{1/5} \left(\frac{w_t}{117\,\mu s}\right)^{1/5}, \tag{11}$$

which is also valid for the X-ray flare fluence to radio fluence ratio. Here, m_* is the particle mass in the upstream medium, m_e is the electron mass (we assume $m_* = m_e$, which is valid for a pair plasma medium), $f_e \equiv n_e/n_{ext}$ is the ratio of the electron density to ion density in the upstream medium (we consider $f_e = 0.5$ for an electron–ion medium), f_ξ is the efficiency of the maser (normalized to a characteristic value of $f_\xi = 10^{-3}$), and v_{centre} is the central frequency of the radio burst. We selected burst B4 for these calculations, instead of the other radio bursts in Extended Data Table 3, since it was the most energetic burst detected from FRB 20200120E, had a well-measured duration, and was covered simultaneously in the soft X-ray band with NICER.

Data availability
The NICER, XMM-Newton, Chandra and NuSTAR data can be accessed from the publicly available HEASARC archive. The data containing radio bursts B1–B9 from FRB 20200120E are available via Zenodo at https://doi.org/10.5281/zenodo.13359005 (ref. 118).

Code availability
The following software packages were used to analyse the data presented in this paper: astropy[98], CIAO[87], dspsr[67], emcee[92], FETCH[69], FTOOLS[83], HEASOFT[84], Heimdall[68], PRESTO[73], SFXC[71], XMM-SAS[85] and XSPEC[25]. The codes used for data processing and producing the figures may be made available from the corresponding author upon reasonable request.

References

1. Lorimer, D. R., Bailes, M., McLaughlin, M. A., Narkevic, D. J. & Crawford, F. A bright millisecond radio burst of extragalactic origin. *Science* **318**, 777–780 (2007).
2. Petroff, E., Hessels, J. W. T. & Lorimer, D. R. Fast radio bursts. *Astron. Astrophys. Rev.* **27**, 4 (2019).

3. Cordes, J. M. & Chatterjee, S. Fast radio bursts: an extragalactic enigma. *Annu. Rev. Astron. Astrophys.* **57**, 417–465 (2019).
4. Platts, E. et al. A living theory catalogue for fast radio bursts. *Phys. Rep.* **821**, 1–27 (2019).
5. Kulkarni, S. R., Ofek, E. O., Neill, J. D., Zheng, Z. & Juric, M. Giant sparks at cosmological distances? *Astrophys. J.* **797**, 70 (2014).
6. Pen, U.-L. & Connor, L. Local circumnuclear magnetar solution to extragalactic fast radio bursts. *Astrophys. J.* **807**, 179 (2015).
7. Pearlman, A. B., Majid, W. A., Prince, T. A., Kocz, J. & Horiuchi, S. Pulse morphology of the galactic center magnetar PSR J1745–2900. *Astrophys. J.* **866**, 160 (2018).
8. The CHIME/FRB Collaboration et al. A bright millisecond-duration radio burst from a Galactic magnetar. *Nature* **587**, 54–58 (2020).
9. Bochenek, C. D. et al. A fast radio burst associated with a Galactic magnetar. *Nature* **587**, 59–62 (2020).
10. Israel, G. L. et al. X-ray and radio bursts from the magnetar 1E 1547.0-5408. *Astrophys. J.* **907**, 7 (2021).
11. Mereghetti, S. et al. INTEGRAL discovery of a burst with associated radio emission from the magnetar SGR 1935+2154. *Astrophys. J. Lett.* **898**, L29 (2020).
12. Li, C. K. et al. HXMT identification of a non-thermal X-ray burst from SGR J1935+2154 and with FRB 200428. *Nat. Astron.* **5**, 378–384 (2021).
13. Ridnaia, A. et al. A peculiar hard X-ray counterpart of a Galactic fast radio burst. *Nat. Astron.* **5**, 372–377 (2021).
14. Tavani, M. et al. An X-ray burst from a magnetar enlightening the mechanism of fast radio bursts. *Nat. Astron.* **5**, 401–407 (2021).
15. The CHIME/FRB Collaboration et al. The CHIME Fast Radio Burst Project: system overview. *Astrophys. J.* **863**, 48 (2018).
16. Bhardwaj, M. et al. A nearby repeating fast radio burst in the direction of M81. *Astrophys. J. Lett.* **910**, L18 (2021).
17. Kirsten, F. et al. A repeating fast radio burst source in a globular cluster. *Nature* **602**, 585–589 (2022).
18. Pilia, M. et al. The lowest-frequency fast radio bursts: Sardinia radio telescope detection of the periodic FRB 180916 at 328 MHz. *Astrophys. J. Lett.* **896**, L40 (2020).
19. Scholz, P. et al. Simultaneous X-ray and radio observations of the repeating fast radio burst FRB 180916.J0158+65. *Astrophys. J.* **901**, 165 (2020).
20. Laha, S. et al. Simultaneous view of FRB 180301 with FAST and NICER during a bursting phase. *Astrophys. J.* **930**, 172 (2022).
21. Majid, W. A. et al. A bright fast radio burst from FRB 20200120E with sub-100 nanosecond structure. *Astrophys. J. Lett.* **919**, L6 (2021).
22. Nimmo, K. et al. Burst timescales and luminosities as links between young pulsars and fast radio bursts. *Nat. Astron.* **6**, 393–401 (2022).
23. Scholz, P. et al. Simultaneous X-ray, gamma-ray, and radio observations of the repeating fast radio burst FRB 121102. *Astrophys. J.* **846**, 80 (2017).
24. HI4PI Collaboration et al. HI4PI: a full-sky H I survey based on EBHIS and GASS. *Astron. Astrophys.* **594**, A116 (2016).
25. Arnaud, K. A. in *Astronomical Data Analysis Software and Systems V* Vol. 101 (eds Jacoby, G. H. & Barnes, J.) 17–20 (Astronomical Society of the Pacific, 1996).
26. Metzger, B. D., Margalit, B. & Sironi, L. Fast radio bursts as synchrotron maser emission from decelerating relativistic blast waves. *Mon. Not. R. Astron. Soc.* **485**, 4091–4106 (2019).
27. Margalit, B., Metzger, B. D. & Sironi, L. Constraints on the engines of fast radio bursts. *Mon. Not. R. Astron. Soc.* **494**, 4627–4644 (2020).
28. Kaspi, V. M. & Beloborodov, A. M. Magnetars. *Annu. Rev. Astron. Astrophys.* **55**, 261–301 (2017).
29. Enoto, T., Kisaka, S. & Shibata, S. Observational diversity of magnetized neutron stars. *Rep. Prog. Phys.* **82**, 106901 (2019).
30. Hurley, K. et al. A giant periodic flare from the soft γ-ray repeater SGR1900+14. *Nature* **397**, 41–43 (1999).
31. Palmer, D. M. et al. A giant γ-ray flare from the magnetar SGR 1806–20. *Nature* **434**, 1107–1109 (2005).
32. Israel, G. L. et al. A Swift gaze into the 2006 March 29 burst forest of SGR 1900+14. *Astrophys. J.* **685**, 1114–1128 (2008).
33. Kouveliotou, C. et al. Multiwavelength observations of the soft gamma repeater SGR 1900+14 during its 2001 April activation. *Astrophys. J. Lett.* **558**, L47–L50 (2001).
34. Younes, G. et al. NICER view of the 2020 burst storm and persistent emission of SGR 1935+2154. *Astrophys. J. Lett.* **904**, L21 (2020).
35. Younes, G. et al. Broadband X-ray burst spectroscopy of the fast-radio-burst-emitting Galactic magnetar. *Nat. Astron.* **5**, 408–413 (2021).
36. Kozlova, A. V. et al. The first observation of an intermediate flare from SGR 1935+2154. *Mon. Not. R. Astron. Soc.* **460**, 2008–2014 (2016).
37. Mereghetti, S., Topinka, M., Rigoselli, M. & Götz, D. INTEGRAL limits on past high-energy activity from FRB 20200120E in M81. *Astrophys. J. Lett.* **921**, L3 (2021).
38. Mereghetti, S. et al. Strong bursts from the anomalous X-ray pulsar 1E 1547.0-5408 observed with the INTEGRAL/SPI anti-coincidence shield. *Astrophys. J. Lett.* **696**, L74–L78 (2009).
39. Olausen, S. A. & Kaspi, V. M. The McGill Magnetar Catalog. *Astrophys. J. Suppl. Ser.* **212**, 6 (2014).
40. Coti Zelati, F., Rea, N., Pons, J. A., Campana, S. & Esposito, P. Systematic study of magnetar outbursts. *Mon. Not. R. Astron. Soc.* **474**, 961–1017 (2018).
41. Yakovlev, D. G. & Pethick, C. J. Neutron star cooling. *Annu. Rev. Astron. Astrophys.* **42**, 169–210 (2004).
42. Pons, J. A. & Rea, N. Modeling magnetar outbursts: flux enhancements and the connection with short bursts and glitches. *Astrophys. J. Lett.* **750**, L6 (2012).
43. Margalit, B., Berger, E. & Metzger, B. D. Fast radio bursts from magnetars born in binary neutron star mergers and accretion induced collapse. *Astrophys. J.* **886**, 110 (2019).
44. Kremer, K., Piro, A. L. & Li, D. Dynamical formation channels for fast radio bursts in globular clusters. *Astrophys. J. Lett.* **917**, L11 (2021).
45. Cordes, J. M. & Wasserman, I. Supergiant pulses from extragalactic neutron stars. *Mon. Not. R. Astron. Soc.* **457**, 232–257 (2016).
46. Lyutikov, M., Burzawa, L. & Popov, S. B. Fast radio bursts as giant pulses from young rapidly rotating pulsars. *Mon. Not. R. Astron. Soc.* **462**, 941–950 (2016).
47. Hankins, T. H., Kern, J. S., Weatherall, J. C. & Eilek, J. A. Nanosecond radio bursts from strong plasma turbulence in the Crab pulsar. *Nature* **422**, 141–143 (2003).
48. Hankins, T. H. & Eilek, J. A. Radio emission signatures in the Crab pulsar. *Astrophys. J.* **670**, 693–701 (2007).
49. Klingler, N. et al. The mouse pulsar wind nebula. *Astrophys. J.* **861**, 5 (2018).
50. Gotthelf, E. V., Safi-Harb, S., Straal, S. M. & Gelfand, J. D. X-ray spectroscopy of the highly magnetized pulsar PSR J1846-0258, its wind nebula, and hosting supernova remnant Kes 75. *Astrophys. J.* **908**, 212 (2021).
51. Tauris, T. M., Sanyal, D., Yoon, S. C. & Langer, N. Evolution towards and beyond accretion-induced collapse of massive white dwarfs and formation of millisecond pulsars. *Astron. Astrophys.* **558**, A39 (2013).
52. Ye, C. S., Kremer, K., Chatterjee, S., Rodriguez, C. L. & Rasio, F. A. Millisecond pulsars and black holes in globular clusters. *Astrophys. J.* **877**, 122 (2019).

53. Soglasnov, V. A. et al. Giant pulses from PSR B1937+21 with widths ≤ 15 nanoseconds and $T_b \geq 5 \times 10^{39}$ K, the highest brightness temperature observed in the universe. *Astrophys. J.* **616**, 439–451 (2004).

54. Main, R., van Kerkwijk, M., Pen, U.-L., Mahajan, N. & Vanderlinde, K. Descattering of giant pulses in PSR B1957+20. *Astrophys. J. Lett.* **840**, L15 (2017).

55. Lee, J. et al. X-ray census of millisecond pulsars in the Galactic field. *Astrophys. J.* **864**, 23 (2018).

56. Sivakoff, G. R., Sarazin, C. L. & Jordán, A. Luminous X-ray flares from low-mass X-ray binary candidates in the early-type galaxy NGC 4697. *Astrophys. J. Lett.* **624**, L17–L20 (2005).

57. Jonker, P. G. et al. Discovery of a new kind of explosive X-ray transient near M86. *Astrophys. J.* **779**, 14 (2013).

58. Irwin, J. A. et al. Ultraluminous X-ray bursts in two ultracompact companions to nearby elliptical galaxies. *Nature* **538**, 356–358 (2016).

59. Chen, H.-Y. et al. Repeating ultraluminous X-ray bursts and repeating fast radio bursts: a possible association? *Astrophys. J.* **937**, 9 (2022).

60. Sridhar, N. et al. Periodic fast radio bursts from luminous X-ray binaries. *Astrophys. J.* **917**, 13 (2021).

61. Deng, C.-M., Zhong, S.-Q. & Dai, Z.-G. An accreting stellar binary model for active periodic fast radio bursts. *Astrophys. J.* **922**, 98 (2021).

62. Bachetti, M. et al. An ultraluminous X-ray source powered by an accreting neutron star. *Nature* **514**, 202–204 (2014).

63. Eftekhari, T. et al. An X-ray census of fast radio burst host galaxies: constraints on active galactic nuclei and X-ray counterparts. *Astrophys. J.* **958**, 66 (2023).

64. Whitney, A., Kettenis, M., Phillips, C. & Sekido, M. VLBI Data Interchange Format (VDIF). In *Sixth Int. VLBI Service for Geodesy and Astron. Proc. from the 2010 Gen. Meet.* (eds Navarro, R. et al.) 192–196 (NASA, 2010).

65. Lazarus, P. et al. Prospects for high-precision pulsar timing with the new Effelsberg PSRIX backend. *Mon. Not. R. Astron. Soc.* **458**, 868–880 (2016).

66. Nimmo, K. et al. A burst storm from the repeating FRB 20200120E in an M81 globular cluster. *Mon. Not. R. Astron. Soc.* **520**, 2281–2305 (2023).

67. van Straten, W. & Bailes, M. DSPSR: digital signal processing software for pulsar astronomy. *Publ. Astron. Soc. Aust.* **28**, 1–14 (2011).

68. Barsdell, B. R., Bailes, M., Barnes, D. G. & Fluke, C. J. Accelerating incoherent dedispersion. *Mon. Not. R. Astron. Soc.* **422**, 379–392 (2012).

69. Agarwal, D., Aggarwal, K., Burke-Spolaor, S., Lorimer, D. R. & Garver-Daniels, N. FETCH: a deep-learning based classifier for fast transient classification. *Mon. Not. R. Astron. Soc.* **497**, 1661–1674 (2020).

70. Kirsten, F. et al. Detection of two bright radio bursts from magnetar SGR 1935+2154. *Nat. Astron.* **5**, 414–422 (2021).

71. Keimpema, A. et al. The SFXC software correlator for very long baseline interferometry: algorithms and implementation. *Exp. Astron.* **39**, 259–279 (2015).

72. Barr, E. D. et al. The Northern High Time Resolution Universe pulsar survey—I. Setup and initial discoveries. *Mon. Not. R. Astron. Soc.* **435**, 2234–2245 (2013).

73. Ransom, S. M. *New Search Techniques for Binary Pulsars*. PhD thesis, Harvard Univ. (2001).

74. The CHIME/Pulsar Collaboration et al. The CHIME Pulsar Project: system overview. *Astrophys. J. Suppl. Ser.* **255**, 5 (2021).

75. Pearlman, A. B., Majid, W. A. & Prince, T. A. Observations of radio magnetars with the deep space network. *Adv. Astron.* **2019**, 6325183 (2019).

76. Pearlman, A. B. et al. Multiwavelength radio observations of two repeating fast radio burst sources: FRB 121102 and FRB 180916. J0158+65. *Astrophys. J. Lett.* **905**, L27 (2020).

77. Pearlman, A. B. et al. Bright X-ray and radio pulses from a recently reactivated magnetar. Preprint at https://arxiv.org/abs/2005.08410v1 (2020).

78. Arzoumanian, Z. et al. The Neutron star Interior Composition Explorer (NICER): mission definition. In *Proc. Space Telescopes and Instrumentation 2014: Ultraviolet to Gamma Ray* (eds Takahashi, T. et al.) 914420 (SPIE, 2014).

79. Gendreau, K. C. et al. The Neutron star Interior Composition Explorer (NICER): design and development. In *Proc. Space Telescopes and Instrumentation 2016: Ultraviolet to Gamma Ray* (eds den Herder, J.-W. A. et al.) 99051H (SPIE, 2016).

80. Prigozhin, G. et al. NICER instrument detector subsystem: description and performance. In *Proc. Space Telescopes and Instrumentation 2016: Ultraviolet to Gamma Ray* (eds den Herder, J.-W. A. et al.) 99051I (SPIE, 2016).

81. Okajima, T. et al. Performance of NICER flight x-ray concentrator. In *Proc. Space Telescopes and Instrumentation 2016: Ultraviolet to Gamma Ray* (eds den Herder, J.-W. A. et al.) 99054X (SPIE, 2016).

82. Gendreau, K. & Arzoumanian, Z. Searching for a pulse. *Nat. Astron.* **1**, 895 (2017).

83. Blackburn, J. K., Shaw, R. A., Payne, H. E., Hayes, J. J. E. & HEASARC. *FTOOLS: A General Package of Software to Manipulate FITS Files* record ascl:9912.002 (Astrophysics Source Code Library, 1999).

84. NASA High Energy Astrophysics Science Archive Research Center (HEASARC). *HEAsoft: Unified Release of FTOOLS and XANADU* record ascl:1408.004 (Astrophysics Source Code Library, 2014).

85. Gabriel, C. et al. in *Astronomical Data Analysis Software and Systems (ADASS) XIII* Vol. 314 (eds Ochsenbein, F. et al.) 759–763 (Astronomical Society of the Pacific, 2004).

86. Wilkes, B. J. & Tananbaum, H. in *Handbook of X-ray and Gamma-ray Astrophysics* (eds Bambi, C. & Santangelo, A.) 1–33 (Springer, Singapore, 2022).

87. Fruscione, A. et al. CIAO: Chandra's data analysis system. In *Proc. Observatory Operations: Strategies, Processes, and Systems* (eds Silva, D. R. & Doxsey, R. E.) 62701V (SPIE, 2006).

88. Scargle, J. D., Norris, J. P., Jackson, B. & Chiang, J. Studies in astronomical time series analysis. VI. Bayesian block representations. *Astrophys. J.* **764**, 167 (2013).

89. Kraft, R. P., Burrows, D. N. & Nousek, J. A. Determination of confidence limits for experiments with low numbers of counts. *Astrophys. J.* **374**, 344–355 (1991).

90. Remillard, R. A. et al. An empirical background model for the NICER X-ray timing instrument. *Astron. J.* **163**, 130 (2022).

91. Goodman, J. & Weare, J. Ensemble samplers with affine invariance. *Commun. Appl. Math. Comput. Sci.* **5**, 65–80 (2010).

92. Foreman-Mackey, D., Hogg, D. W., Lang, D. & Goodman, J. Emcee: the MCMC Hammer. *Publ. Astron. Soc. Pac.* **125**, 306–312 (2013).

93. Mushotzky, R. F., Cowie, L. L., Barger, A. J. & Arnaud, K. A. Resolving the extragalactic hard X-ray background. *Nature* **404**, 459–464 (2000).

94. Campana, R., Orlandini, M., Del Monte, E., Feroci, M. & Frontera, F. The radiation environment in a low Earth orbit: the case of BeppoSAX. *Exp. Astron.* **37**, 599–613 (2014).

95. Bartels, J. The standardized index, K_s, and the planetary index, K_p. *Int. Assoc. Terr. Magn. Electr. Bull.* **12b**, 97–120 (1949).

96. Kaastra, J. S. & Bleeker, J. A. M. Optimal binning of X-ray spectra and response matrix design. *Astron. Astrophys.* **587**, A151 (2016).

97. Buccheri, R. et al. Search for pulsed γ-ray emission from radio pulsars in the COS-B data. *Astron. Astrophys.* **128**, 245–251 (1983).

98. The Astropy Collaboration et al. Astropy: a community Python package for astronomy. *Astron. Astrophys.* **558**, A33 (2013).

99. The Planck Collaboration. Planck 2018 results. VI. Cosmological parameters. *Astron. Astrophys.* **641**, A6 (2020).

100. Bernadich, M. C. I., Schwope, A. D., Kovlakas, K., Zezas, A. & Traulsen, I. An expanded ultraluminous X-ray source catalogue. *Astron. Astrophys.* **659**, A188 (2022).

101. Kaaret, P., Feng, H. & Roberts, T. P. Ultraluminous X-ray sources. *Annu. Rev. Astron. Astrophys.* **55**, 303–341 (2017).

102. Avakyan, A. et al. XRBcats: Galactic low-mass X-ray binary catalogue. *Astron. Astrophys.* **675**, A199 (2023).

103. Neumann, M., Avakyan, A., Doroshenko, V. & Santangelo, A. XRBcats: Galactic High Mass X-ray Binary Catalogue. *Astron. Astrophys.* **677**, A134 (2023).

104. Rea, N. et al. The first outburst of the new magnetar candidate SGR 0501+4516. *Mon. Not. R. Astron. Soc.* **396**, 2419–2432 (2009).

105. Hu, C.-P. et al. NICER observation of the temporal and spectral evolution of Swift J1818.0-1607: a missing link between magnetars and rotation-powered pulsars. *Astrophys. J.* **902**, 1 (2020).

106. Enoto, T. et al. A month of monitoring the new magnetar Swift J1555.2-5402 during an X-ray outburst. *Astrophys. J. Lett.* **920**, L4 (2021).

107. Younes, G. et al. X-ray burst and persistent emission properties of the magnetar SGR 1830-0645 in outburst. *Astrophys. J.* **924**, 136 (2022).

108. Crider, A. A magnetar flare in the BATSE Catalog? *Am. Inst. Phys. Conf. Proc.* **836**, 64–67 (2006).

109. Ofek, E. O. et al. The Short-Hard GRB 051103: observations and implications for its nature. *Astrophys. J.* **652**, 507–511 (2006).

110. Frederiks, D. D. et al. On the possibility of identifying the short hard burst GRB 051103 with a giant flare from a soft gamma repeater in the M81 group of galaxies. *Astron. Lett.* **33**, 19–24 (2007).

111. Mazets, E. P. et al. A giant flare from a soft gamma repeater in the Andromeda Galaxy (M31). *Astrophys. J.* **680**, 545–549 (2008).

112. Burns, E. et al. Identification of a local sample of gamma-ray bursts consistent with a magnetar giant flare origin. *Astrophys. J. Lett.* **907**, L28 (2021).

113. Svinkin, D. et al. A bright γ-ray flare interpreted as a giant magnetar flare in NGC 253. *Nature* **589**, 211–213 (2021).

114. Younes, G. et al. Simultaneous NuSTAR/Chandra observations of the bursting pulsar GRO J1744-28 during its third reactivation. *Astrophys. J.* **804**, 43 (2015).

115. Bagnoli, T., in't Zand, J. J. M., D'Angelo, C. R. & Galloway, D. K. A population study of type II bursts in the Rapid Burster. *Mon. Not. R. Astron. Soc.* **449**, 268–287 (2015).

116. Moon, D.-S., Eikenberry, S. S. & Wasserman, I. M. SMC X-1 as an intermediate-stage flaring X-ray pulsar. *Astrophys. J. Lett.* **582**, L91–L94 (2003).

117. Galloway, D. K. et al. The Multi-INstrument Burst ARchive (MINBAR). *Astrophys. J. Suppl. Ser.* **249**, 32 (2020).

118. Pearlman, A. B. et al. Multiwavelength constraints on the origin of a nearby repeating fast radio burst source in a globular cluster (public data release). *Zenodo* https://doi.org/10.5281/zenodo.13359005 (2024).

119. An, H. et al. NuSTAR observations of X-ray bursts from the magnetar 1E 1048.1-5937. *Astrophys. J.* **790**, 60 (2014).

120. Coti Zelati, F. et al. The new magnetar SGR J1830-0645 in outburst. *Astrophys. J. Lett.* **907**, L34 (2021).

121. Hurley, K. et al. An exceptionally bright flare from SGR 1806–20 and the origins of short-duration γ-ray bursts. *Nature* **434**, 1098–1103 (2005).

122. Freedman, W. L. et al. The Hubble Space Telescope Extragalactic Distance Scale Key Project. I. The discovery of cepheids and a new distance to M81. *Astrophys. J.* **427**, 628–655 (1994).

123. Lin, L. et al. No pulsed radio emission during a bursting phase of a Galactic magnetar. *Nature* **587**, 63–65 (2020).

124. Tendulkar, S. P., Kaspi, V. M. & Patel, C. Radio nondetection of the SGR 1806–20 giant flare and implications for fast radio bursts. *Astrophys. J.* **827**, 59 (2016).

125. Ryder, S. D. et al. A luminous fast radio burst that probes the Universe at redshift 1. *Science* **382**, 294–299 (2023).

Acknowledgements

Author contributions

A.B.P. is the lead author of the paper and wrote the majority of the paper. A.B.P. prepared the figures, with significant contributions

from P.S. A.B.P. and P.S. led the astrophysical interpretation of the results from this study. A.B.P. coordinated the data analyses. A.B.P. led the analysis of the NICER data of FRB 20200120E, with significant contributions from P.S. P.S. led the analysis of the XMM-Newton, NuSTAR and Chandra data of FRB 20200120E, with significant contributions from A.B.P., and wrote the corresponding sections of the paper. S.B. and L.G.S. searched the ToO Effelsberg data for radio bursts from FRB 20200120E. A.B.P., P.S., S.B. and L.G.S. analysed the properties of the radio bursts detected from FRB 20200120E during the ToO Effelsberg observations. P.S., L.G.S. and A.B.P. coordinated the simultaneous X-ray and radio observations with XMM-Newton and Effelsberg. P.S. and L.G.S. coordinated the simultaneous X-ray and radio observations with NuSTAR, Chandra and Effelsberg. A.B.P. and K.N. measured the properties and arrival times of the radio bursts detected from FRB 20200120E during the PRECISE observations. A.B.P. analysed the simultaneous NICER and Effelsberg data obtained during the PRECISE observational campaign. A.B.P., F.K. and J.W.T.H. coordinated the NICER and Effelsberg observations during the PRECISE campaign. A.B.P. and K.N. coordinated the NICER observations during an independent radio monitoring campaign of FRB 20200120E with Effelsberg. A.B.P. performed the searches for radio bursts from FRB 20200120E in the CHIME/Pulsar radio data. A.B.P., C.M.T. and E.F. coordinated the radio observations of FRB 20200120E with CHIME/Pulsar. A.B.P. and B.W.M. performed the flux calibration of the CHIME/Pulsar data. V.M.K. played a significant leadership role that enabled these results. All other co-authors contributed comments that helped improve the paper. A.B.P. is the Principal Investigator (PI) of the Guest Observer (GO) Cycle 2 and 3 NICER programmes dedicated to performing simultaneous X-ray and radio observations of nearby repeating FRBs. P.S. is the PI of the XMM-Newton, NuSTAR and Chandra X-ray follow-up programmes of FRB 20200120E. P.S. is the PI of the ToO Effelsberg radio observing programme of nearby repeating FRB sources.

Competing interests

The authors declare no competing interests.

Additional information

Extended data is available for this paper at https://doi.org/10.1038/s41550-024-02386-6.

Supplementary information The online version contains supplementary material available at https://doi.org/10.1038/s41550-024-02386-6.

Correspondence and requests for materials should be addressed to Aaron B. Pearlman.

Peer review information *Nature Astronomy* thanks Marilyn Cruces and the other, anonymous, reviewer(s) for their contribution to the peer review of this work.

Reprints and permissions information is available at www.nature.com/reprints.

Publisher's note Springer Nature remains neutral with regard to jurisdictional claims in published maps and institutional affiliations.

Aaron B. Pearlman [1,2,3] ✉, Paul Scholz [4,5], Suryarao Bethapudi [6], Jason W. T. Hessels [1,2,7,8], Victoria M. Kaspi [1,2], Franz Kirsten [8,9], Kenzie Nimmo [10], Laura G. Spitler [6], Emmanuel Fonseca [11,12], Bradley W. Meyers [13,14], Ingrid H. Stairs [14], Chia Min Tan [1,2,13], Mohit Bhardwaj [15], Shami Chatterjee [16], Amanda M. Cook [4,17], Alice P. Curtin [1,2], Fengqiu Adam Dong [14], Tarraneh Eftekhari [18], B. M. Gaensler [4,17,19], Tolga Güver [20,21], Jane Kaczmarek [22,23], Calvin Leung [24], Kiyoshi W. Masui [10,25], Daniele Michilli [10,25], Thomas A. Prince [3], Ketan R. Sand [1,2], Kaitlyn Shin [10,25], Kendrick M. Smith [26] & Shriharsh P. Tendulkar [27,28,29]

[1]Department of Physics, McGill University, Montréal, Québec, Canada. [2]Trottier Space Institute, McGill University, Montréal, Québec, Canada. [3]Division of Physics, Mathematics, and Astronomy, California Institute of Technology, Pasadena, CA, USA. [4]Dunlap Institute for Astronomy and Astrophysics, University of Toronto, Toronto, Ontario, Canada. [5]Department of Physics and Astronomy, York University, Toronto, Ontario, Canada. [6]Max-Planck-Institut für Radioastronomie, Bonn, Germany. [7]Anton Pannekoek Institute for Astronomy, University of Amsterdam, Amsterdam, The Netherlands. [8]ASTRON, Netherlands Institute for Radio Astronomy, Dwingeloo, The Netherlands. [9]Department of Space, Earth and Environment, Chalmers University of Technology, Onsala Space Observatory, Onsala, Sweden. [10]MIT Kavli Institute for Astrophysics and Space Research, Massachusetts Institute of Technology, Cambridge, MA, USA. [11]Department of Physics and Astronomy, West Virginia University, Morgantown, WV, USA. [12]Center for Gravitational Waves and Cosmology, Chestnut Ridge Research Building, West Virginia University, Morgantown, WV, USA. [13]International Centre for Radio Astronomy Research, Curtin University, Bentley, Western Australia, Australia. [14]Department of Physics and Astronomy, University of British Columbia, Vancouver, British Columbia, Canada. [15]McWilliams Center for Cosmology, Department of Physics, Carnegie Mellon University, Pittsburgh, PA, USA. [16]Cornell Center for Astrophysics and Planetary Science, Cornell University, Ithaca, NY, USA. [17]David A. Dunlap Department of Astronomy and Astrophysics, University of Toronto, Toronto, Ontario, Canada. [18]Center for Interdisciplinary Exploration and Research in Astrophysics, Department of Physics and Astronomy, Northwestern University, Evanston, IL, USA. [19]Department of Astronomy and Astrophysics, University of California Santa Cruz, Santa Cruz, CA, USA. [20]Department of Astronomy and Space Sciences, Science Faculty, Istanbul University, Istanbul, Turkey. [21]Istanbul University Observatory Research and Application Center, Istanbul University, Istanbul, Turkey. [22]CSIRO Space and Astronomy, Parkes Observatory, Parkes, New South Wales, Australia. [23]Department of Computer Science, Math, Physics, and Statistics, University of British Columbia, Okanagan Campus, Kelowna, British Columbia, Canada. [24]Department of Astronomy, University of California Berkeley, Berkeley, CA, USA. [25]Department of Physics, Massachusetts Institute of Technology, Cambridge, MA, USA. [26]Perimeter Institute for Theoretical Physics, Waterloo, Ontario, Canada. [27]Department of Astronomy and Astrophysics, Tata Institute of Fundamental Research, Mumbai, India. [28]National Centre for Radio Astronomy, Pune, India. [29]CIFAR Azrieli Global Scholars Program, MaRS Centre, Toronto, Ontario, Canada. ✉e-mail: aaron.b.pearlman@physics.mcgill.ca
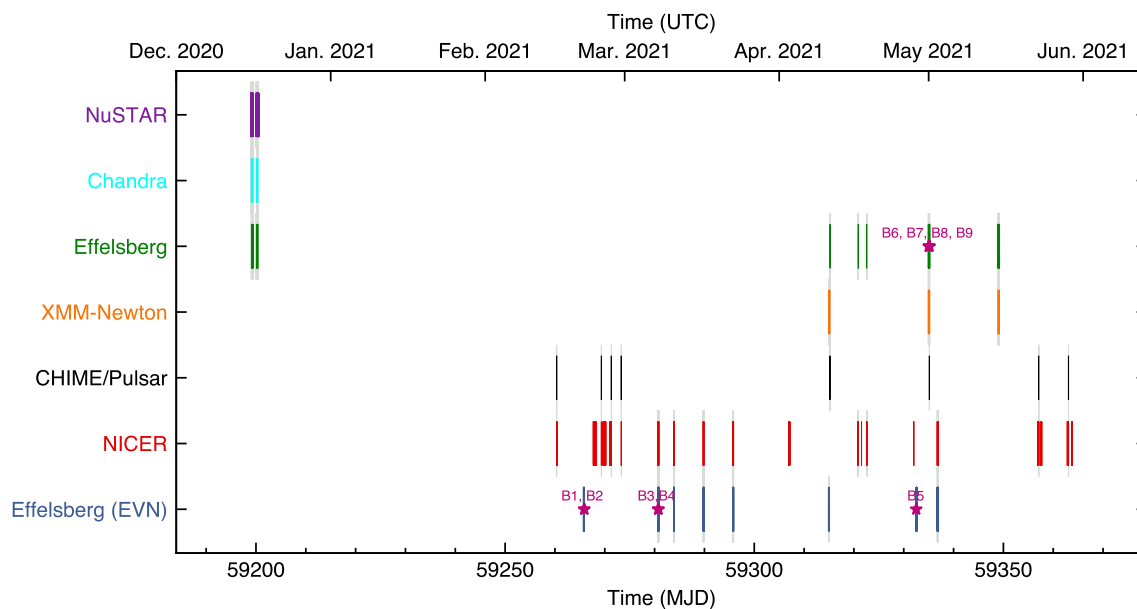
Extended Data Fig. 1 | Timeline of X-ray and radio observations of FRB 20200120E performed between 2020 December and 2021 June. The coloured rectangles indicate the start time, end time, and duration of each observation. X-ray observations carried out with NuSTAR, Chandra, XMM-Newton, and NICER are labelled using purple, cyan, orange, and red rectangles, respectively. The green rectangles correspond to independent observations carried out with the Effelsberg radio telescope, and the blue rectangles indicate radio observations performed with Effelsberg during interferometric observations with radio telescopes from the European Very Long Baseline Interferometry (VLBI) Network (EVN). Radio observations carried out with the CHIME/Pulsar system are shown using black rectangles. The shaded grey regions highlight times when multiple X-ray and radio instruments were used to perform simultaneous observations. The barycentric arrival times of the radio bursts, shown in Fig. 1, are labelled using magenta stars.
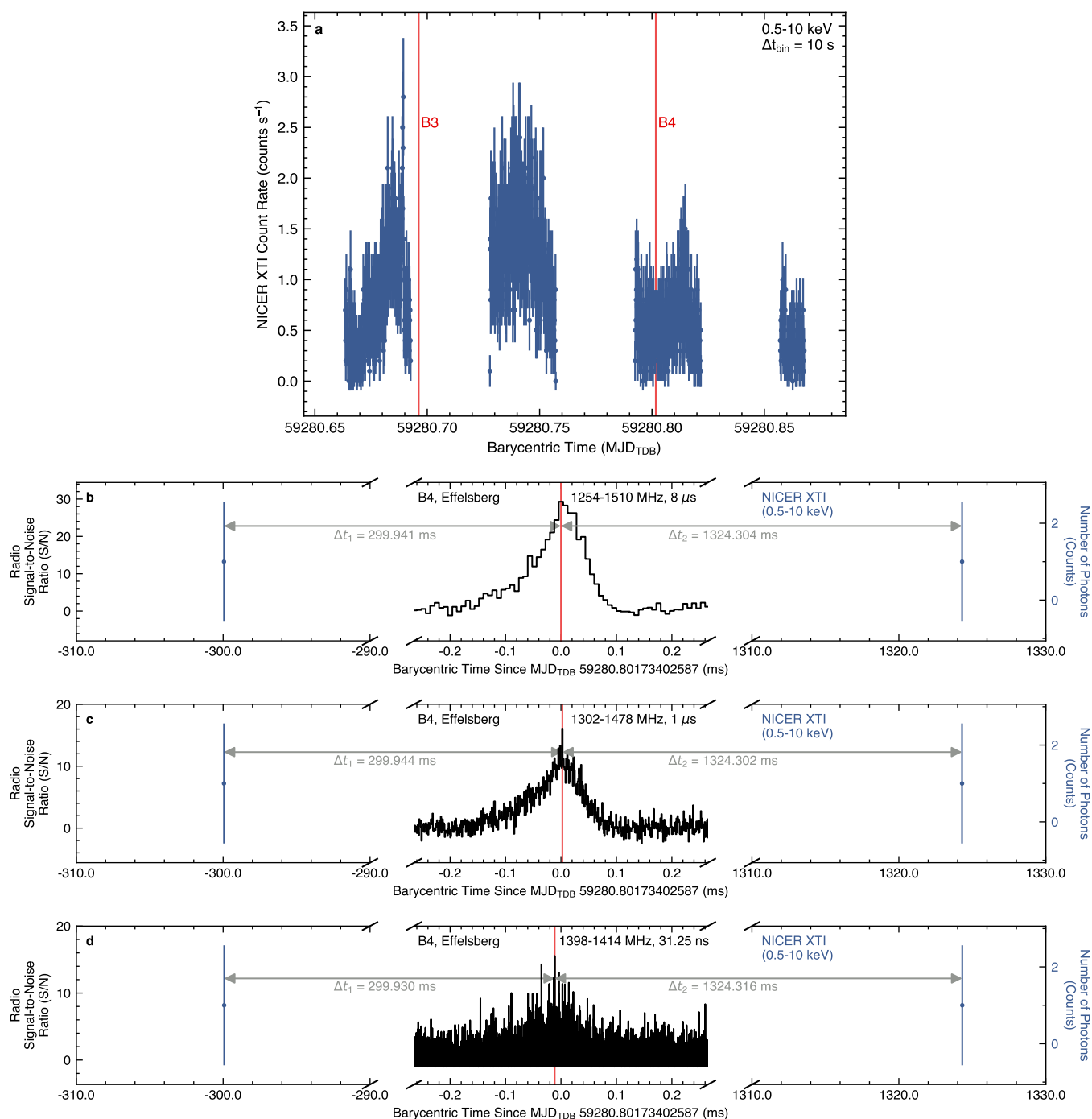
Extended Data Fig. 2 | X-ray and radio light curves from simultaneous NICER and Effelsberg observations of FRB 20200120E, covering bursts B3 and B4. Panel **a**: NICER 0.5–10 keV light curve, shown with time bin widths of 10 s. The error bars correspond to 1σ Poisson uncertainties on the count rates. The barycentric arrival times of bursts B3 and B4 are indicated by the vertical red lines. Panel **b**: Frequency-summed burst profile of B4, detected using the Effelsberg radio telescope in the 1254–1510 MHz frequency range and shown at a time resolution of 8 μs. Panel **c**: Frequency-summed burst profile of B4 in the 1302–1478 MHz frequency range, shown at a time resolution of 1 μs. Panel **d**: Frequency-summed burst profile of B4 in the 1398–1414 MHz frequency range, shown at a time resolution of 31.25 ns. The X-ray photons detected closest in time to burst B4 with NICER in the 0.5–10 keV energy band are also shown in panels **b**–**d**, along with 1σ Poisson uncertainties based on the photon counts. The time differences between the nearest X-ray photons and the peak barycentric arrival time of burst B4 are labelled using grey arrows. The vertical red lines in panels **b**–**d** indicate the peak barycentric arrival time of burst B4 in each frequency range.
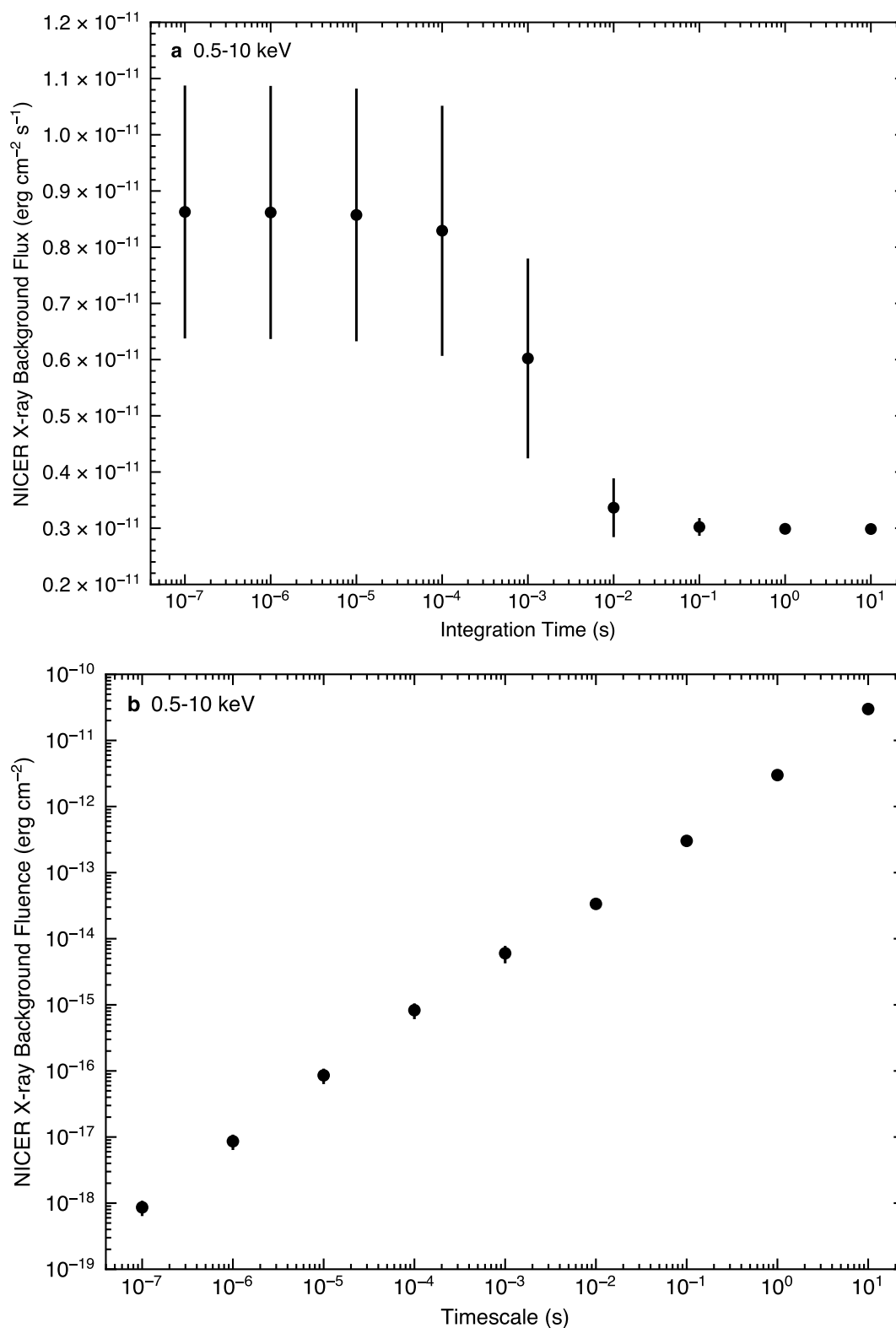
Extended Data Fig. 3 | Average background X-ray flux and fluence from NICER observations of blank sky regions. Panel **a** shows the average absorbed background X-ray flux from NICER in the 0.5–10 keV energy band on timescales ranging from 100 ns to 10 s, and panel **b** shows the corresponding X-ray fluence on these timescales. These measurements were obtained by assuming an X-ray spectrum with a photon index of $\Gamma = 1.4$, similar to that of the diffuse X-ray background[93], and a hydrogen column density of $N_{\mathrm{H}} = 6.73 \times 10^{20}$ cm^{-2} towards FRB 20200120E[24]. The error bars shown in panels **a** and **b** correspond to 1σ uncertainties (Methods).
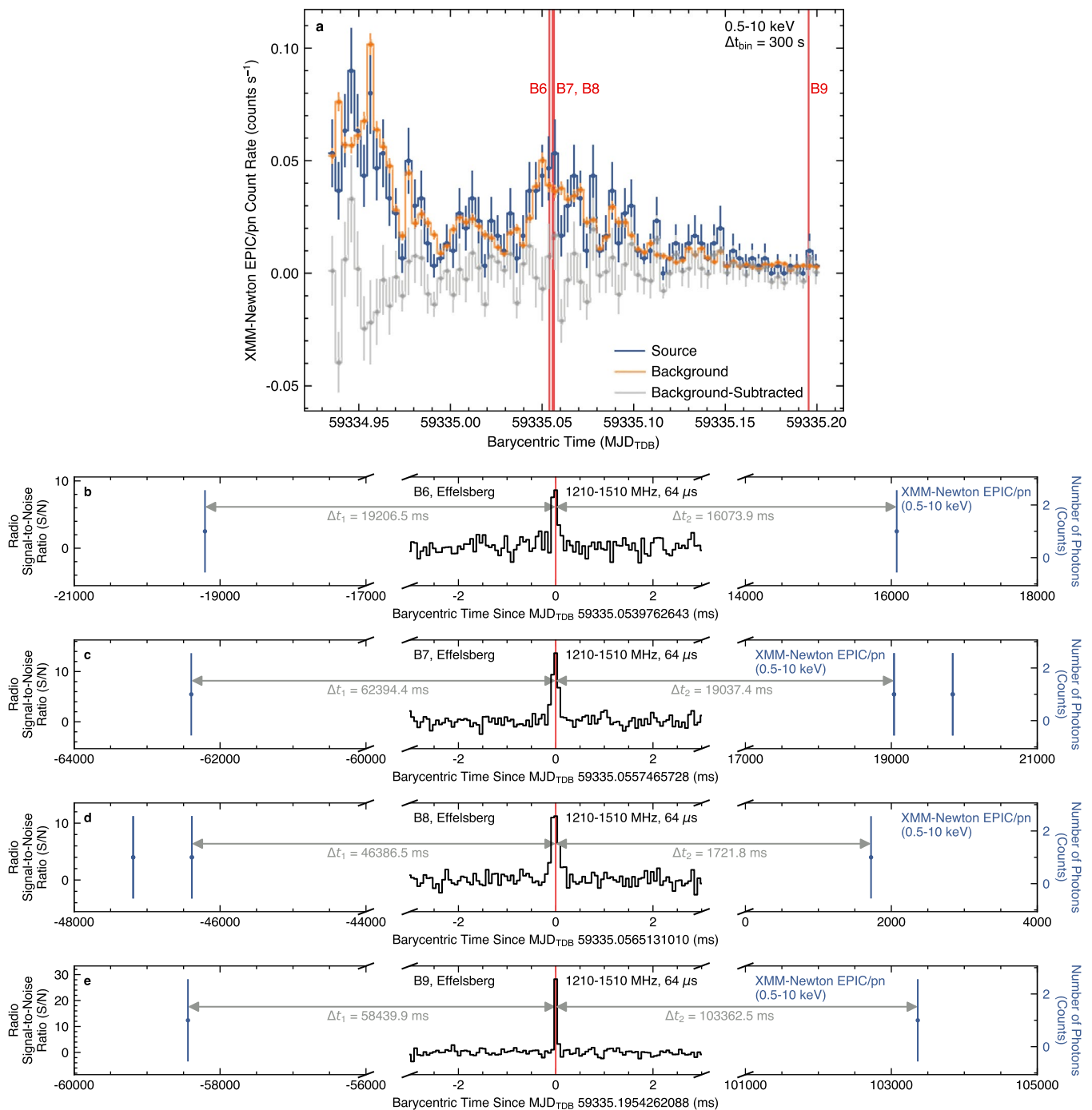
Extended Data Fig. 4 | X-ray and radio light curves from simultaneous XMM-Newton EPIC/pn and Effelsberg observations of FRB 20200120E, covering bursts B6, B7, B8, and B9. Panel **a**: Source, background, and background-subtracted 0.5–10 keV light curves of FRB 20200120E from XMM-Newton's EPIC/pn camera. The light curves are shown with time bin widths of 300 s, and the error bars correspond to 1σ Poisson uncertainties on the count rates. The barycentric arrival times of bursts B6, B7, B8, and B9 are indicated by the vertical red lines. Panels **b**–**e**: Frequency-summed burst profiles of B6, B7, B8, and B9, detected using the Effelsberg radio telescope in the 1210–1510 MHz frequency range and shown at a time resolution of 64 μs. The X-ray photons detected closest in time to these radio bursts with XMM-Newton's EPIC/pn camera in the 0.5–10 keV energy band are also shown in panels **b**–**e**, along with 1σ Poisson uncertainties based on the photon counts. The time differences between the nearest X-ray photons and the peak barycentric arrival times of the radio bursts are labelled using grey arrows. The vertical red lines indicate the peak barycentric arrival times of the radio bursts.
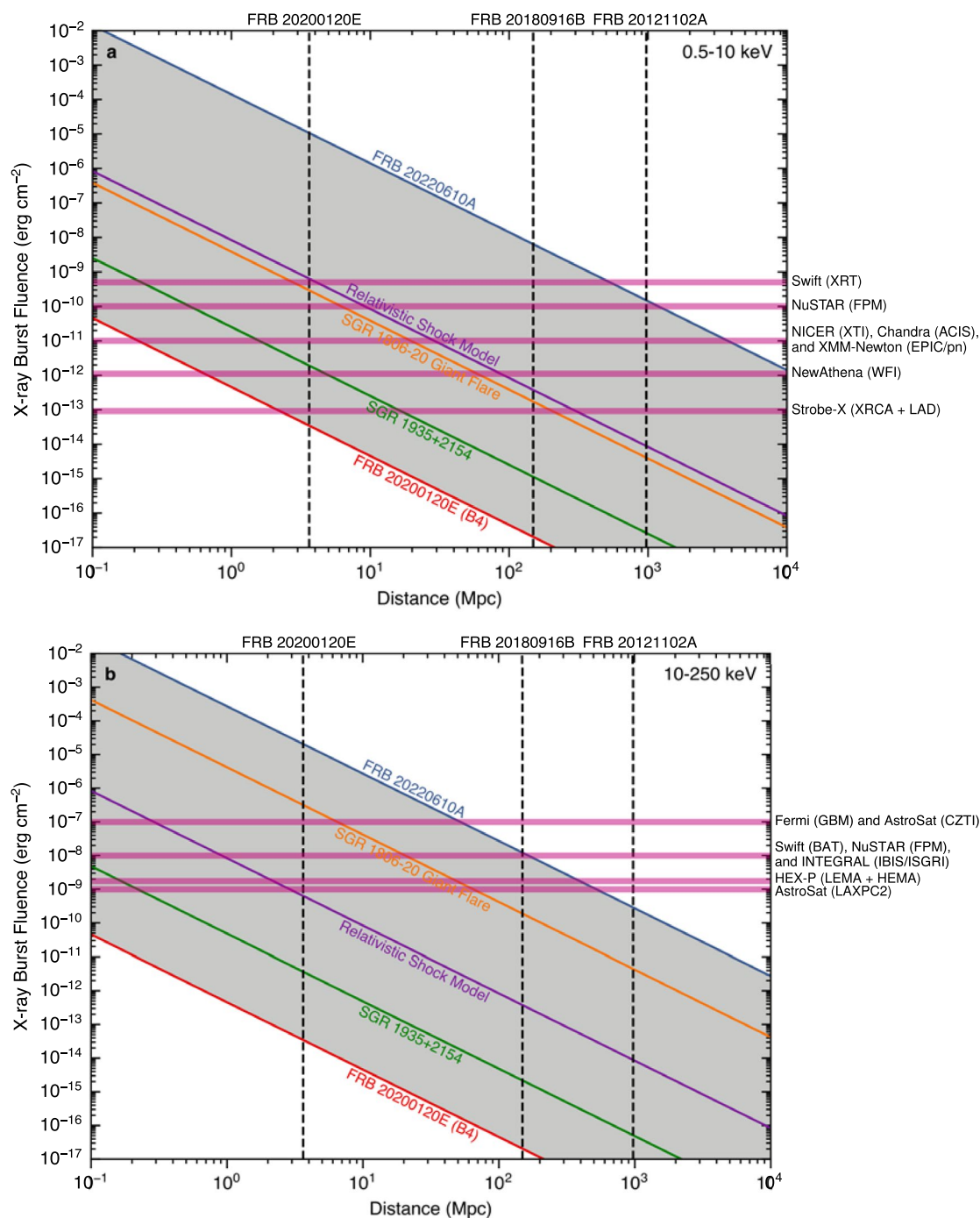
Extended Data Fig. 5 | Detectability of X-ray counterparts from FRB sources located at distances between 100 kpc and 10 Gpc with current and future X-ray instruments. Panel **a** shows the predicted X-ray burst fluences in the soft X-ray band (0.5–10 keV), and panel **b** shows the predicted X-ray burst fluences in the hard X-ray band (10–250 keV). The red lines show predictions for bursts similar to B4 from FRB 20200120E. The blue lines indicate the expected X-ray fluences for FRB 20220610A-like radio bursts[125]. The red and blue lines in each energy band are derived by scaling the measured radio fluences by an X-ray-to-radio fluence ratio based on the X-ray and radio fluences observed from the FRB-like burst detected on 28 April 2020 from SGR 1935+2154[8,9,12]. The green lines are also derived from X-ray and radio burst fluence measurements at the time of FRB-like activity on 28 April 2020 from SGR 1935+2154[8,9,12]. The orange lines show the predicted X-ray fluences for giant flares similar to the 27 December 2004 flare observed from SGR 1806−20[31]. The purple lines correspond to predictions from the relativistic shock model[26,27] for a fiducial X-ray flare energy of $E_{\text{flare}} = 10^{42}$ erg. The distances of three repeating FRB sources (FRB 20200120E, FRB 20180916B, and FRB 20121102A) are indicated by the vertical dashed black lines. The horizontal magenta lines correspond to nominal 3σ X-ray burst fluence detection thresholds for a selection of current (AstroSat, Chandra, Fermi, INTEGRAL, NICER, NuSTAR, Swift, and XMM-Newton) and future (HEX-P, NewAthena, and Strobe-X) X-ray instruments.

Extended Data Table 1 | Radio observations of FRB 20200120E

Telescope	Start Time[a] (UTC)	End Time[b] (UTC)	Mid-time[c] (MJD)	Exposure[d] (min)	Time Resolution[e] (μs)	Frequency Resolution[f] (MHz)	Observing Backend[g]	Number of Radio Bursts Detected
Effelsberg	2020-12-16 02:07:43	2020-12-16 10:08:54	59199.25577	480.0	54.0	0.59	PFFTS & EDD	0
Effelsberg	2020-12-17 02:13:59	2020-12-17 09:14:57	59200.23921	420.0	54.0	0.59	PFFTS & EDD	0
CHIME	2021-02-15 07:56:44	2021-02-15 08:35:07	59260.34439	38.4	327.68	0.390625	Pulsar	0
Effelsberg	2021-02-20 17:07:57	2021-02-20 21:47:06	59265.81078	162.0	0.03125	16.0	PSRIX & VLBI	2
CHIME	2021-02-24 07:21:19	2021-02-24 07:59:47	59269.31983	38.5	327.68	0.390625	Pulsar	0
CHIME	2021-02-26 07:13:28	2021-02-26 07:51:54	59271.31436	38.4	327.68	0.390625	Pulsar	0
CHIME	2021-02-28 07:05:40	2021-02-28 07:44:03	59273.30893	38.4	327.68	0.390625	Pulsar	0
Effelsberg	2021-03-07 15:52:58	2021-03-07 20:32:09	59280.75872	162.2	0.03125	16.0	PSRIX & VLBI	2
Effelsberg	2021-03-10 19:08:05	2021-03-10 23:48:28	59283.89464	161.2	0.03125	16.0	PSRIX & VLBI	0
Effelsberg	2021-03-16 18:20:01	2021-03-16 22:43:46	59289.85548	148.9	0.03125	16.0	PSRIX & VLBI	0
Effelsberg	2021-03-22 16:20:37	2021-03-22 20:44:06	59295.77247	149.3	0.03125	16.0	PSRIX & VLBI	0
Effelsberg	2021-04-10 21:18:40	2021-04-10 23:18:12	59314.92947	73.3	0.03125	16.0	PSRIX & VLBI	0
CHIME	2021-04-11 04:20:14	2021-04-11 04:58:37	59315.19404	38.4	40.96	0.390625	Pulsar	0
Effelsberg	2021-04-11 04:35:02	2021-04-11 05:28:26	59315.20954	53.4	65.5	0.24	PSRIX	0
Effelsberg	2021-04-16 19:52:19	2021-04-16 22:05:31	59320.87425	133.2	65.5	0.24	PSRIX	0
Effelsberg	2021-04-18 12:20:10	2021-04-18 14:20:10	59322.55567	120.0	65.5	0.24	PSRIX	0
Effelsberg	2021-04-28 11:07:57	2021-04-28 15:42:43	59332.55926	172.6	0.03125	16.0	PSRIX & VLBI	1
Effelsberg	2021-04-30 21:55:38	2021-05-01 05:15:39	59335.06642	436.6	64.0	0.78125	EDD	4
CHIME	2021-05-01 03:01:50	2021-05-01 03:40:16	59335.13962	38.4	40.96	0.390625	Pulsar	0
Effelsberg	2021-05-02 17:08:07	2021-05-02 23:35:57	59336.84863	240.5	0.03125	16.0	PSRIX & VLBI	0
Effelsberg	2021-05-14 21:21:06	2021-05-15 05:22:30	59349.05681	480.0	64.0	0.78125	EDD	0
CHIME	2021-05-23 01:35:06	2021-05-23 02:13:29	59357.07937	38.4	40.96	0.390625	Pulsar	0
CHIME	2021-05-29 01:11:31	2021-05-29 01:49:54	59363.06299	38.4	40.96	0.390625	Pulsar	0

Radio bursts were detected from FRB 20200120E during the observations highlighted in bold. [a]Start time of the observation. [b]End time of the observation. [c]Mid-time of the observation. [d]Total exposure time. [e]Time resolution of the channelized data used to search for radio bursts. For Effelsberg observations performed during the PRECISE observing campaign, we list the native time resolution (31.25 ns) of the voltage data recorded with the VLBI backend. [f]Frequency resolution of the channelized data used to search for radio bursts. For Effelsberg observations performed during the PRECISE observing campaign, we list the bandwidth of the subbands (16 MHz) recorded with the VLBI backend. [g]Observing backend used during the observation. Observations with two listed backends indicate that data were simultaneously recorded using both backends.

Extended Data Table 2 | X-ray observations of FRB 20200120E

Telescope	Observation ID	Start Time[a]	End Time[b]	Mid-time[c]	Exposure[d]	Count Rate[e]	Off-axis Angle[f]	3σ Persistent X-ray Flux Upper Limit[g]
		(UTC)	(UTC)	(MJD)	(s)	(counts s^{-1})	(arcmin)	(F_X, 10^{-13} erg cm^{-2} s^{-1})
Chandra	9540	2008-08-24 09:51:41	2008-08-24 17:35:52	54702.57207	25724	1.40×10^{-3}	13.78	< 0.1
NuSTAR	80701506002	2020-12-15 23:26:09	2020-12-16 10:01:09	59199.19698	23774	0.13	0.17	< 1
Chandra	23544	2020-12-16 01:02:35	2020-12-16 09:53:28	59199.22780	30695	1.63×10^{-4}	0.30	< 0.06
NuSTAR	80701506004	2020-12-17 02:11:09	2020-12-17 12:51:09	59200.31330	21963	0.13	0.17	< 2
Chandra	24894	2020-12-17 02:17:05	2020-12-17 09:17:29	59200.24117	24071	8.31×10^{-5}	0.28	< 0.06
NICER	3658040101	2021-02-15 08:17:39	2021-02-15 10:00:20	59260.38124	2011	0.61	0.58	< 3
NICER	3658040102	2021-02-22 07:54:16	2021-02-22 23:09:00	59267.64697	5899	0.60	0.56	< 0.5
NICER	3658040103	2021-02-23 00:22:19	2021-02-23 06:54:00	59268.15149	4850	0.78	0.58	< 4
NICER	3658040104	2021-02-24 07:21:38	2021-02-24 23:11:20	59269.63645	6840	3.24	0.57	< 11
NICER	3658040105	2021-02-25 00:18:16	2021-02-25 23:59:40	59270.50623	6299	1.27	0.55	< 6
NICER	3658040106	2021-02-26 01:02:19	2021-02-26 07:45:40	59271.18332	6343	0.54	0.56	< 0.7
NICER	3658040107	2021-02-28 07:21:19	2021-02-28 07:55:40	59273.31840	1933	0.58	0.66	< 2
NICER	**3658040108**	2021-03-07 15:48:32	2021-03-07 20:45:10	59280.76170	8503	0.81	0.55	< 1
NICER	4689010101	2021-03-10 19:44:49	2021-03-10 23:27:00	59283.89993	5925	0.44	0.54	< 0.4
NICER	4689010102	2021-03-16 18:16:05	2021-03-16 22:03:20	59289.84007	5363	0.51	0.53	< 0.1
NICER	4689010103	2021-03-22 16:44:00	2021-03-22 20:26:30	59295.77448	7087	0.65	0.50	< 0.6
NICER	4689010104	2021-04-02 23:47:35	2021-04-03 03:20:10	59307.06519	6068	1.63	0.49	< 0.4
XMM-Newton	0872392401	2021-04-10 22:59:32	2021-04-11 05:04:49	59315.08484	17300[h]	5.66×10^{-3}	0.53	< 0.07
NICER	4689010105	2021-04-16 20:46:09	2021-04-16 21:15:47	59320.87567	1360	18.81[i]	0.35	< 3
NICER	4689010106	2021-04-17 12:28:59	2021-04-17 12:51:40	59321.52800	1242	1.45	0.01	< 1
NICER	4689010107	2021-04-18 13:01:19	2021-04-18 13:38:00	59322.55532	1772	1.04	0.35	< 3
NICER	4689010108	2021-04-27 22:53:04	2021-04-27 23:19:00	59331.96252	1198	0.45	0.02	< 0.3
XMM-Newton	**0872392501**	2021-04-30 21:51:57	2021-05-01 05:03:57	59335.06108	7285[h]	8.78×10^{-3}	0.53	< 0.2
NICER	4689010109	2021-05-02 17:23:04	2021-05-02 22:22:30	59336.82832	2108	0.37	0.06	< 0.08
XMM-Newton	0872392601	2021-05-14 21:00:24	2021-05-15 05:02:20	59349.04262	15429[h]	7.19×10^{-3}	0.53	< 0.1
NICER	3658040109	2021-05-22 20:35:00	2021-05-22 22:44:27	59356.90259	4172	0.68	0.09	< 1
NICER	3658040110	2021-05-22 23:38:55	2021-05-23 17:20:22	59357.35392	12616	0.74	0.06	< 0.6
NICER	3658040111	2021-05-28 19:03:15	2021-05-28 22:54:09	59362.87410	7557	0.48	0.02	< 0.7
NICER	3658040112	2021-05-28 23:41:41	2021-05-29 20:02:40	59363.41123	10211	0.66	0.03	< 0.7

Radio bursts were detected from FRB 20200120E during the observations highlighted in bold. FRB 20200120E was observed with NICER for a total exposure time of 109.4 ks between 15 February 2021 and 30 May 2021. The total exposure times of the Chandra, NuSTAR, and XMM-Newton observations of FRB 20200120E were 80.5 ks, 45.7 ks, and 40.0 ks, respectively. [a]Start time of the observation. [b]End time of the observation. [c]Mid-time of the observation. [d]Total exposure time during Good Time Intervals (GTIs). [e]Average (non-background-subtracted) count rate during GTIs. The count rates are derived in the 0.5–10 keV energy band for the Chandra, NICER, and XMM-Newton observations and in the 3–79 keV energy band for the NuSTAR observations. A circular region around the source, centred on the position of FRB 20200120E from VLBI[17], was used to measure the count rates for the Chandra, NuSTAR, and XMM-Newton observations. [f]Off-axis angle, calculated relative to the nominal pointing direction and the VLBI position of FRB 20200120E[17]. [g]3σ persistent X-ray flux upper limits are derived in the 0.5–10 keV energy band for the Chandra, NICER, and XMM-Newton observations and in the 3–79 keV energy band for the NuSTAR observations. A fiducial absorbed power-law spectral model, with $N_H = 6.73 \times 10^{20}$ cm^{-2} (ref. 24) and $\Gamma = 2$, was used to calculate the persistent X-ray flux upper limits. [h]Total exposure time after removal of instrumental flares. [i]The higher count rate compared to other NICER observations was due to higher background, as indicated by larger housekeeping parameter (`FPM_OVERONLY_COUNT`) values.

Extended Data Table 3 | Measured properties of radio bursts detected from FRB 20200120E with the Effelsberg radio telescope at 1.4 GHz

Burst ID[a]	Time of Arrival (ToA) at Burst Peak[b] (t_{peak}, MJD$_{TDB}$)	Peak S/N[c] (S/N)$_{peak}$	Dispersion Measure[d] (DM, pc cm^{-3})	Width[e] (w_t, μs)	Frequency Extent[f] (w_f, MHz)	Peak Flux Density[g] (F_R, Jy)	Fluence[g,h] ($\mathcal{F}_R$, Jy ms)	Luminosity[i] (L_R, 10^{37} erg s^{-1})	Energy[j] (E_R, 10^{32} erg)
B1	59265.88304442095	6.6	87.75	156 ± 1	140 ± 1	1.59 ± 0.32	0.13 ± 0.03	0.3 ± 0.1	5.1 ± 1.5
B2	59265.88600917244	36.1	87.75	62 ± 1, 93 ± 0.5[k]	103 ± 1, 89 ± 1[k]	8.71 ± 1.74	0.63 ± 0.13	1.6 ± 0.5	25.1 ± 7.0
B3	59280.69618750235	64.8	87.75	46.7 ± 0.1	94 ± 1	15.6 ± 3.12	0.53 ± 0.11	4.5 ± 1.2	20.9 ± 5.8
B4	59280.80173402587	29.3	87.75	117 ± 1	134 ± 1	7.07 ± 1.41	0.71 ± 0.14	2.4 ± 0.7	28.0 ± 7.6
B5	59332.50446582513	6.9	87.75	56.6 ± 0.1	86 ± 1	1.66 ± 0.33	0.09 ± 0.02	0.6 ± 0.2	3.6 ± 1.0
B6	59335.0539762643	8.6	87.76	92 ± 11	53.9 ± 0.8	0.66 ± 0.10	0.10 ± 0.02	0.5 ± 0.1	4.9 ± 1.2
B7	59335.0557465728	13.7	87.76	107 ± 8	72.7 ± 0.8	1.05 ± 0.16	0.17 ± 0.03	0.7 ± 0.2	7.9 ± 1.9
B8	59335.0565131010	11.2	87.76	124 ± 10	87.5 ± 0.8	0.86 ± 0.13	0.17 ± 0.02	0.6 ± 0.2	7.8 ± 1.9
B9	59335.1954262088	28.2	87.76 ± 0.06	46 ± 4	135.2 ± 0.8	2.16 ± 0.32	0.19 ± 0.03	2.0 ± 0.5	9.1 ± 2.2

[a]The properties of bursts B1, B2, B3, B4, and B5 were measured using data sampled at a time resolution of 8 μs[22]. The properties of bursts B6, B7, B8, and B9 were determined from data recorded with a time resolution of 64 μs. [b]Barycentric time at the peak of the burst, determined after removing the time delay due to dispersion and correcting to infinite frequency. The barycentric times were derived using the Jet Propulsion Laboratory (JPL) DE405 ephemeris and the position of FRB 20200120E (α_{J2000} = 09^{h}57^{m}54.69935^s, δ_{J2000} = 68°49'00.8529")[17], measured in the International Celestial Reference Frame (ICRF) from VLBI. A dispersion constant of $\mathcal{D}$ = 1/(2.41 × 10^{-4}) MHz^2 pc^{-1} cm^3 s was used to correct the burst ToAs for dispersion. The burst ToAs were calculated using the Barycentric Dynamical Time (TDB) standard. We present refined barycentric ToAs for bursts B1, B2, B3, B4, and B5, compared to those listed in refs. 17 and 22, since an incorrect position for FRB 20200120E was used during the barycentring procedure in these earlier studies. [c]Signal-to-noise ratio (S/N) at the burst peak. [d]The properties of bursts B1, B2, B3, B4, and B5 were measured using a dispersion measure (DM) of 87.75 pc cm^{-3} (ref. 22). The DM of burst B9 corresponds to the value that maximized the peak S/N. The properties of bursts B6, B7, and B8 were derived using the S/N-optimized DM obtained from B9. [e]Temporal width of each burst. The width of bursts B1, B2, B3, B4, and B5 is defined as the full-width at half-maximum (FWHM) divided by $\sqrt{2}$ of a two-dimensional (2D) Gaussian fit to the 2D autocorrelation function (ACF)[22]. The width of bursts B6, B7, and B9 is defined as the FWHM divided by $\sqrt{2}$ of a Gaussian fit to the dedispersed, frequency-summed burst profile. [f]Frequency extent of each burst. The frequency extent of bursts B1, B2, B3, B4, and B5 is defined as the FWHM divided by $\sqrt{2}$ of a 2D Gaussian fit to the 2D ACF[22]. The frequency extent of bursts B6, B7, B8, and B9 was determined by eliminating frequency channels until the 'on-pulse' data were consistent with noise. [g]The errors associated with these measurements are based on a conservative estimate of the uncertainty on the system equivalent flux density (SEFD) of the Effelsberg radio telescope at the time of these observations. We estimate a 20% uncertainty on Effelsberg's SEFD at the time of bursts B1, B2, B3, B4, and B5, and a 15% uncertainty on Effelsberg's SEFD at the time of bursts B6, B7, B8, and B9. [h]Fluences of the radio bursts were computed using the ±2σ temporal width region. [i]Isotropic-equivalent radio luminosity values were calculated using the expression $L_R = 4\pi d^2 \mathcal{F}_R / (w_t(1 + z))$, where d = 3.63 ± 0.34 Mpc[122] corresponds to the distance of FRB 20200120E, $\mathcal{F}_R$ is the fluence of the radio burst, w_t is the temporal width of the radio burst, and z is the redshift of FRB 20200120E. [j]Isotropic-equivalent energy values were calculated using the expression $E_R = 4\pi d^2 \mathcal{F}_R / (1 + z)$, where d is the distance of FRB 20200120E, $\mathcal{F}_R$ is the fluence of the radio burst, and z is the redshift of FRB 20200120E. [k]Values measured from each burst component.

Extended Data Table 4 | NICER background measurements on 100 ns to 10 s timescales in the 0.5–10 keV energy band

Timescale	$\langle N_{bkg}^{blank}\rangle$ [a] (counts)	N_{bkg}^{sw} [b] (counts)	$N_{bkg}^{100\,s}$ [c] (counts)
10 s	8.53 ± 0.04	8.1 ± 0.2	4.9 ± 0.5
1 s	0.85 ± 0.01	0.81 ± 0.2	0.49 ± 0.05
100 ms	0.086 ± 0.004	0.081 ± 0.02	0.049 ± 0.005
10 ms	0.010 ± 0.001	0.0081 ± 0.002	0.0049 ± 0.0005
1 ms	0.0017 ± 0.0005	$(8.1 \pm 0.2) \times 10^{-4}$	$(4.9 \pm 0.5) \times 10^{-4}$
100 μs	$(2.4 \pm 0.6) \times 10^{-4}$	$(8.1 \pm 0.2) \times 10^{-5}$	$(4.9 \pm 0.5) \times 10^{-5}$
10 μs	$(2.4 \pm 0.6) \times 10^{-5}$	$(8.1 \pm 0.2) \times 10^{-6}$	$(4.9 \pm 0.5) \times 10^{-6}$
1 μs	$(2.5 \pm 0.6) \times 10^{-6}$	$(8.1 \pm 0.2) \times 10^{-7}$	$(4.9 \pm 0.5) \times 10^{-7}$
100 ns	$(2.5 \pm 0.6) \times 10^{-7}$	$(8.1 \pm 0.2) \times 10^{-8}$	$(4.9 \pm 0.5) \times 10^{-8}$

[a]Average number of background photons in the 0.5–10 keV energy band, derived from NICER observations of blank sky fields. [b]Number of background photons in the 0.5–10 keV energy band, derived from the NICER 'Space Weather' model[90]. [c]Inferred number of background photons based on the count rate within ±100 s of the barycentric, infinite frequency peak time of burst B4 (t_{peak}^{B4}), assuming all detected photons are attributed to the background.

Extended Data Table 5 | Observed fluences of the X-ray burst associated with the FRB-like radio burst detected from SGR 1935+2154 on 28 April 2020 and predicted X-ray fluences in the 0.5–10 keV and 3–79 keV energy bands for a similar X-ray burst emitted from the location of FRB 20200120E

Instrument	Observed X-ray Fluence from SGR 1935+2154[a] (Absorbed / Unabsorbed) ($\mathcal{F}_X$, 10^{-7} erg cm^{-2})	Predicted X-ray Fluence from FRB 20200120E[b] (Absorbed / Unabsorbed) ($\mathcal{F}_X$, 10^{-12} erg cm^{-2}, 0.5–10 keV)	Predicted X-ray Fluence from FRB 20200120E[c] (Absorbed / Unabsorbed) ($\mathcal{F}_X$, 10^{-12} erg cm^{-2}, 3–79 keV)	References
AGILE	$(5^{+10}_{-4})^{d}$ / $(5^{+10}_{-4})^{d}$	$(0.6^{+0.6}_{-0.3})$ / $(0.6^{+0.6}_{-0.3})$	(6^{+11}_{-5}) / (6^{+11}_{-5})	[14]
Insight-HXMT	$(6.4^{+0.4}_{-0.3})^{e}$ / $(7.1^{+0.4}_{-0.4})^{e}$	$(1.9^{+0.1}_{-0.1})$ / $(2.0^{+0.1}_{-0.1})$	$(3.9^{+0.2}_{-0.2})$ / $(3.9^{+0.2}_{-0.2})$	[12]
INTEGRAL	$(6.1^{+0.3}_{-0.3})^{f}$ / $(6.1^{+0.3}_{-0.3})^{f}$	$(0.55^{+0.03}_{-0.03})$ / $(0.57^{+0.03}_{-0.03})$	$(4.1^{+0.2}_{-0.2})$ / $(4.1^{+0.2}_{-0.2})$	[11]
Konus-Wind	$(9.7^{+0.4}_{-0.4})^{g}$ / $(9.7^{+0.4}_{-0.4})^{g}$	$(0.60^{+0.02}_{-0.02})$ / $(0.61^{+0.03}_{-0.03})$	$(5.0^{+0.2}_{-0.2})$ / $(5.0^{+0.2}_{-0.2})$	[13]

Predicted X-ray fluence values at the distance of FRB 20200120E (3.63 ± 0.34 Mpc[122]) were calculated using the best-fit (exponentially cut-off power-law) spectral models in refs. 11–14 for SGR 1935+2154. We assumed a fiducial distance of 10 kpc to SGR 1935+2154 and hydrogen column densities of N_H = 2.79 ×10^{22} cm^{-2} (ref. 12) and N_H = 6.73 ×10^{20} cm^{-2} (ref. 24) towards SGR 1935+2154 and FRB 20200120E, respectively. [a]Absorbed and unabsorbed X-ray fluences are derived from best-fit spectral models for SGR 1935+2154. [b]Predicted absorbed and unabsorbed X-ray fluences in the 0.5–10 keV energy band. [c]Predicted absorbed and unabsorbed X-ray fluences in the 3–79 keV energy band. [d]Measured X-ray fluence in the 18–60 keV energy band. [e]Measured X-ray fluence in the 1–250 keV energy band. [f]Measured X-ray fluence in the 20–200 keV energy band. [g]Measured X-ray fluence in the 20–500 keV energy band.